Fuel-Optimal Guidance for End-to-End Human-Mars Entry, Powered-Descent, and Landing Mission

Changhuang Wan, Gangshan Jing, Ran Dai, and Jeremy R. Rea

Abstract

This paper investigates the fuel-optimal guidance problem of the end-to-end human-Mars entry, powered descent, and landing (EDL) mission. It applies a unified modeling scheme and develops a computationally efficient new optimization algorithm to solve the multi-phase optimal guidance problem. The end-to-end EDL guidance problem is first modeled as a multi-phase optimal control problem with different dynamics and constraints at each phase. Via polynomial approximation and discretization techniques, this multi-phase optimal control problem is then reformulated as a polynomial programming problem. By introducing intermediate variables and quadratic equality constraints, a polynomial program is equivalently converted into a nonconvex quadratically constrained quadratic program (QCQP). Then, a novel customized alternating direction method of multipliers (ADMM) is proposed to efficiently solve the large-scale QCQP with convergence proof to a local optimum under certain conditions on the algorithmic parameters. The fuel savings under the end-to-end human-Mars EDL guidance are verified by comparing to the fuel consumption using the separate phase guidance approach. Furthermore, the computational efficiency of the customized ADMM algorithm is validated by comparing to the state-of-the-art nonlinear programming method. The robustness of the customized ADMM algorithm is verified via extensive simulation cases with random initial conditions.

Index Terms

human-Mars EDL, Trajectory optimization, ADMM

A human-Mars mission requires the delivery of a payload from the entry interface at hypersonic speed to a preflight-designated surface location at near-zero speed with pinpoint precision, defined as landing within one hundred meters of the location [1]. Unlike past robotic landing missions, the predicted mass of a human-scale entry vehicle will increase at least an order of magnitude. For example, the entry vehicle in Mars Science Laboratory Mission weighs around 2,400 kg [2]. In contrast, the designed vehicles for human-scale Mars landing mission weigh over 50 tons [3]. As a result, the entry vehicle has to fly with a higher L/D ratio and then powered-descent will replace parachute in robotic landing mission to achieve precise landing by generating retro-thrusts at supersonic speed to decelerate the human-scale landers [4].

Changhuang Wan is with the Department of Aerospace Science Engineering, Tuskegee University, Tuskegee, AL 36088, USA cwan@tuskegee.edu

Gangshan Jing is with the Department of Electrical and Computer Engineering, North Carolina State University, Raleigh, NC, 27695, USA nameisjing@gmail.com

Ran Dai is with the School of Aeronautics and Astronautics at Purdue University, randai@purdue.edu

Jeremy R. Rea is Subsystem Manager, Flight Mechanics and Trajectory Design Branch, NASA Johnson Space Center, Houston, TX, 77058

In the past decades, guidance methods for EDL missions have gained extensive development, with some of them implemented in successful flight tests. While great success for small-scale robotic landing missions has been achieved, a human-Mars EDL mission is very different in scale, operation, and challenges [1], [5], [6]. First, few efforts pay attention to optimizing the entry phase guidance maneuvers that lead to an ideal initial condition for the powered descent operation. Moreover, the existing literature generally focuses on generating guidance commands separately at each phase instead of planning the entire mission as a whole [7]. Practically, control of aerodynamic forces will improve the deceleration capability of the entry vehicle, which benefits fuel saving during the following powered descent phase. Existing entry guidance algorithms are traditionally tailored to the L/D ratio of the vehicle, including high L/D [8], [9], mid to low L/D [10], [11], and others [12], [13], [14]. A unified guidance method has been developed for a wide range of entry vehicles with varying lifting capabilities [15]. However, few of these works consider how to optimize entry guidance maneuvers to minimize fuel consumption in the following powered descent phase and also improve the landing accuracy. Thus, an entry trajectory that is optimized via modulations of aerodynamic forces to provide an ideal initial condition of the powered descent phase holds potential to further reduce the fuel consumption and consequently the mass of the landing vehicle needed for the mission.

Both direct and indirect optimization methods have been developed to solve EDL related problems. The indirect methods need to simplify the vehicle dynamics under certain assumptions to generate onboard trajectories with much reduced computational loads [16], [17], [18], [19], [20]. When complicated inequality/equality constraints are considered, indirect methods are not applicable to those EDL missions. Nonlinear programming (NLP), e.g., sequential quadratic programming [21], [22], [23], [24], classified as a direct method, has been applied to solve entry and supersonic gliding problems, where a continuous-time optimal control problem is converted into a parameter optimization problem via discretization. With nonconvexity involved in the objective or constraints or both, convergence to an optimal solution cannot be guaranteed from NLP, and it generally requires a good initial guess of the unknown variables. Recent efforts have applied second order cone programming to solve both entry and powered descent problems by combining successive linearization and relaxation techniques to generate optimization-based guidance commands [25], [26], [27]. In addition, work in [28] combined the pseudospectral optimal control and convex optimization for the powered descent and landing problem.

In this paper, the two dimensional (2D) end-to-end EDL mission will be considered and an advanced guidance method for both fuel-optimal and precise landing will be developed. Specifically, the EDL problem is modeled as a multi-phase optimal control problem with varying dynamics and constraints at each phase. To solve this challenging problem, a computationally efficient modeling scheme is developed to convert the EDL guidance problem at each phase into a unified representation. Then an implementable and convergent optimization algorithm is designed. Firstly, all non-polynomial functions, e.g., the atmosphere density model, are approximated by continuous or piece-wise continuous polynomials. Then, via the discretization techniques, the EDL problem of each phase is reformulated as a polynomial programming problem. By introducing extra variables and quadratic constraints, every polynomial program can be expressed as an equivalent nonconvex quadratically constrained quadratic programming (QCQP) problem [29].

It is known that a QCQP is equivalent to a linear matrix programming problem by introducing a to-be-determined rank-one matrix [30], [31]. Due to the nonconvex and nonlinear nature of the rank-one constraint, the converted problem is still NP-hard

[31]. Extensive relaxation methods have been developed to find a lower bound on the objective value of a QCQP, which are not guaranteed to yield a feasible solution [32], [33], [34]. The alternating direction method of multipliers (ADMM) is a well-known sequential algorithm that divides the unknown variables into two sets and solves them separately in an alternative sequence when solving both sets jointly is more complicated. The fundamental principle of ADMM is to formulate the augmented Lagrangian and then find the first order conditions of optimality for the two unknown sets in an alternating sequence, followed by updating the Lagrange multipliers associated with equality constraints [35], [36]. Convergence has been proven for ADMM in some special nonconvex optimization problems [37], [38].

Motivated by the advantages of ADMM, we divide variables in QCQPs into two sets and solve them separately in an alternating sequence. The customized ADMM significantly reduces the computational efforts required to solve every iterative problem, which is applicable to the large-scale EDL problem. Our prior work in [39], [40] has developed an implementable optimization algorithm based on ADMM to solve nonconvex QCQPs. In this paper, we further improve the computational performance in terms of convergence and reduce the computational complexity by using a set of switching functions to represent the quadratic inequalities in a QCQP, which does not require using the slack variables associated with inequalities.

Compared with our former work of end-to-end EDL guidance presented in [40], this paper extends our former work from three aspects: (i) A more precise model for the entry dynamics is applied in this paper, which considers the quadratic relationship between the lift and drag coefficients instead of the linear one used in [40]. In addition, a new normalization scale is applied to the entry dynamics to improve the numerical accuracy of the converged results from the customized ADMM. (ii) For the proposed customized ADMM, a rigorous convergence proof is provided based on mild conditions on algorithmic parameters. (iii) In the simulation section, robustness analysis of the proposed algorithm is presented through extensive simulation cases.

The main contributions of this paper can be summarized as follows:

- The end-to-end EDL guidance problem for human Mars mission is modeled as a multi-phase optimal control problem with different dynamics and constraints in each phase. To our best knowledge, it is the first time that the entry phase guidance and the powered descent phase guidance are combined as an integrated problem to increase the flexibility when searching for an optimal solution for the entire EDL guidance problem. The benefits on fuel-saving of the end-to-end formulation are verified by simulations comparing to the separate phase guidance strategy.
- To handle the large-scale multi-phase optimal control problem, we apply a unified modeling scheme to convert the nonlinear end-to-end EDL guidance problem into a nonconvex QCQP via polynomial approximation and discretization, which reduces the non-linearity and complexity of the original problem formulation.
- We propose a new customized ADMM to solve large-scale nonconvex QCQPs, where inequality constraints are represented by switching functions. Moreover, the convergence proof of the customized ADMM under certain conditions on the algorithmic parameters is provided. The computational efficiency of the customized ADMM is validated via comparative simulation results from a commercial NLP solver. Furthermore, the robustness of the customized ADMM is validated via extensive simulation cases.

This paper is organized as follows. §I introduces the formulation of the end-to-end human-Mars EDL mission as a multi-phase optimal control problem and the transformation from the optimal control problem into a homogeneous QCQP. §II presents

the framework and convergence analysis of the customized ADMM to search for the optimal solution of general nonconvex QCQPs. In §III, numerical results for the separate phase guidance and the end-to-end guidance problems, comparative results from an NLP solver, and robustness analysis of the customized ADMM are provided. Conclusions are presented in §IV.

I. Problem Formulation

In human-Mars missions, the vehicle is required to deorbit, enter, descend and land softly at a specific mission site with high precision. The entire EDL mission can be divided into two major phases, an entry phase and a powered descent phase. In this section, the formulation of the optimal guidance problems for both phases are presented separately and then integrated into an entire fuel-optimal EDL guidance problem subject to dynamic constraints, mission constraints, and continuity constraints between these two phases. By applying the discretization technique and introducing additional variables, the fuel-optimal EDL guidance problem is converted into a nonconvex QCQP problem. This uniform modeling scheme can be applied to general multi-phase mission planning problems as well as the three-dimensional EDL guidance problems.

A. Optimal Guidance for the Entry Phase

In the entry phase, the motion of a point-mass entry vehicle is usually described in a Cartesian coordinate system with the origin of the coordinate located at the center of Mars. The two degree of freedom (2-DoF) dimensionless equations of motion for the entry vehicle over a spherical non-rotating Mars are expressed as

$$\begin{aligned} \dot{R} &= V\sin\gamma, \\ \dot{V} &= -D - \frac{\sin\gamma}{(Rh_0/R_m)^2}, \\ \dot{\gamma} &= \frac{1}{V}\left(L + V^2\frac{\cos\gamma}{R} - \frac{\cos\gamma}{(Rh_0/R_m)^2}\right), \end{aligned} \tag{1}$$

where R is the radial distance between the entry vehicle and the Mars center, V is the vehicle speed, and γ is the relative flight path angle, R_m is the radius of Mars. In the above dimensionless formulation, length is normalized by $h_0 = 100$ km, and time is normalized by $\sqrt{h_0/g_0}$ ($g_0 = 3.711\,\text{m/sec}^2$ is the gravity acceleration of Mars). Accordingly, the speed term is normalized by $\sqrt{h_0 g_0}$. D and L are the normalized aerodynamic drag and lift, respectively, defined by

$$D = \frac{1}{2}S\rho C_D V^2, \tag{2a}$$

$$L = \frac{1}{2}S\rho C_L V^2, \tag{2b}$$

where ρ is the Mars atmosphere density, determined by a nonlinear function of altitude, S is the reference area of the entry vehicle, C_D and C_L are the aerodynamic drag and lift coefficients. Note that, ρ is normalized by $\frac{m_0}{h_0}$, where m_0 is the initial mass of the entry vehicle. In this paper, we assume that $C_D = c_{d_0} + c_{d_1}C_L + c_{d_2}C_L^2$ holds for the entry vehicle, where c_{d_0}, c_{d_1} and c_{d_2} are the constant coefficients. During the entry phase, C_L is handled as the control variable. Moreover, three types of trajectory constraints are considered during the entry phase.

1) Stagnation-point convective heating load constraint:

$$\dot{Q} = k_Q \sqrt{\frac{\rho}{R_{\text{nose}}}} V^{3.15} \leq \dot{Q}_{\max}, \tag{3}$$

where R_{nose} is the nose radius of the vehicle, k_Q is a constant depending on the composition of the Martian atmosphere, $\dot{Q}_{\max}$ denotes the allowable peak heating rate. This inequality constrains the heating rate at a stagnation point on the surface of the vehicle with a curvature radius R_{nose} [15].

2) Dynamic pressure constraint:

$$\bar{q} = \frac{g_0 m_0 \rho V^2}{2} \leq \bar{q}_{\max}, \tag{4}$$

where $\bar{q}_{\max}$ is the allowable peak dynamic pressure.

3) Normal load constraint:

$$\sqrt{L^2 + D^2} \leq n_{\max}, \tag{5}$$

where $n_{\max}$ is the allowable normal load on the surface of the entry vehicle.

At the end of the entry phase, the entry vehicle is required to descend to an altitude within a specified range. The optimal guidance problem for the entry phase is expressed as

$$\begin{aligned}
&\min_{C_L, t_I} \; V(t_I), \\
&\text{subject to } \dot{R} = V \sin\gamma, \\
&\quad \dot{V} = -D - \frac{\sin\gamma}{(Rh_0/R_m)^2}, \\
&\quad \dot{\gamma} = \frac{1}{V}\left(L + V^2 \frac{\cos\gamma}{R} - \frac{\cos\gamma}{(Rh_0/R_m)^2}\right), \\
&\quad \dot{Q} = k_Q \sqrt{\frac{\rho}{R_{\text{nose}}}} V^{3.15} \leq \dot{Q}_{\max}, \\
&\quad \bar{q} = \frac{g_0 m_0 \rho V^2}{2} \leq \bar{q}_{\max}, \\
&\quad \sqrt{L^2 + D^2} \leq n_{\max}, \\
&\quad D = \frac{1}{2} S \rho C_D V^2, \\
&\quad L = \frac{1}{2} S \rho C_L V^2, \\
&\quad C_D = c_{d_0} + c_{d_1} C_L + c_{d_2} C_L^2, \\
&\quad R(t_0) = R_0, \; V(t_0) = V_0, \; \gamma(t_0) = \gamma_0, \\
&\quad R_I^L \leq R(t_I) \leq R_I^U,
\end{aligned} \tag{6}$$

where t_I is the time at the end of the entry phase and it is unknown, and R_I^L and R_I^U are the lower and upper bounds on the terminal radius, respectively. The objective function during the entry phase is the final speed since a smaller speed at the end of the entry phase is supposed to require less propellant during the powered descent phase to decelerate the vehicle to zero

speed. After the entry phase, the retro-propulsion system will be ignited to start the powered descent phase.

B. Fuel-Optimal Guidance for the Powered Descent Phase

In the powered descent phase, the vehicle will be decelerated by using a retro-propulsion system and land at a preflight-designated site on the Mars surface with near-zero speed. To simplify the expression, the equations of motion during the powered descent phase are analyzed in a Cartesian coordinate system with its origin fixed at a point on the Mars' surface. Without loss of generality, we assume the origin of the Cartesian coordinate is located at the landing point. The 2-DoF dimensionless dynamic equations during the powered-descent phase is expressed as

$$\dot{\mathbf{r}} = \mathbf{v}, \tag{7a}$$

$$\dot{\mathbf{v}} = \mathbf{g} + \frac{\mathbf{T}}{m}, \tag{7b}$$

$$\dot{m} = -\eta \|\mathbf{T}\|_2, \tag{7c}$$

where $\mathbf{r} = [x, z]^T$ is the position vector of the landing vehicle, $\mathbf{v} = [v_x, v_z]^T$ denotes the velocity vector, $\mathbf{g} = [0, -g_0]^T$ is the gravity acceleration vector, $\mathbf{T} = [T_x, T_z]^T$ denotes the thrust vector, m is the landing vehicle mass, and η represents the specific exhaust velocity of the rockets, which is assumed to be a constant. In the above dimensionless formulation, length is normalized by 1000 m, velocity is normalized by 100 m/sec, and mass is normalized by 1000 kg. As a result, time is normalized by 10 sec, acceleration is normalized by 10 m/sec^2, and thrust is normalized by 10000 N. The magnitude of thrust $\mathbf{T}$ during the powered descent phase is bounded by

$$T_{\min} \leq \|\mathbf{T}(t)\|_2 \leq T_{\max}, \ \forall t \in [t_I, t_f], \tag{8}$$

where t_I is the time at the end of the entry phase, which also denotes the rocket ignition time, i.e. the starting time of the powered descent phase, and t_f is the final time at the end of the mission. Due to the limited fuel, the constraint on the vehicle mass is expressed as

$$m(t_I) = m_{\text{pdi}}, \ m(t_f) \geq m_{\text{dry}}, \tag{9}$$

where m_{pdi} is the gross mass of the vehicle at the beginning of the powered descent phase, and m_{dry} is the structural mass. Meanwhile, to prevent the landing vehicle from impacting the Mars surface before landing, a glide-slope constraint is considered for the powered-descent trajectory, which is expressed as

$$\mathbf{r} \in \mathcal{C} := \left\{ \mathbf{r} \in \mathbb{R}^2 : \frac{\mathbf{r} \cdot \mathbf{e}}{\|\mathbf{r}\| \|\mathbf{e}\|} \geq \cos\theta \right\}, \tag{10}$$

where $\mathbf{e}$ is a unit vector along the z axis and θ is the maximum glide-slope angle. As the aerodynamic forces are generally much smaller than the thrust generated by the retro-propulsion system during the powered descent phase, the aerodynamic effects during the powered descent phase are ignored. Then the fuel-optimal guidance problem for the powered descent phase

is expressed as

$$\min_{\mathbf{T},t_f} \int_{t_I}^{t_f} \dot{m}\, \mathrm{d}t \tag{11}$$

$$\begin{aligned}
\text{subject to } & \dot{\mathbf{r}} = \mathbf{v}, \\
& \dot{\mathbf{v}} = \mathbf{g} + \frac{\mathbf{T}}{m}, \\
& \dot{m} = -\eta \|\mathbf{T}\|_2, \\
& T_{\min} \le \|\mathbf{T}\|_2 \le T_{\max},\ \forall t \in [t_I, t_f], \\
& \mathbf{r} \in \mathcal{C} := \left\{ \mathbf{r} \in \mathbb{R}^2 : \frac{\mathbf{r}\cdot\mathbf{e}}{\|\mathbf{r}\|\|\mathbf{e}\|} \ge \cos\theta \right\}, \\
& m(t_I) = m_{\text{pdi}},\ m(t_f) \ge m_{\text{dry}}, \\
& \mathbf{r}(t_I) = \mathbf{r}_0,\ \mathbf{v}(t_f) = \mathbf{v}_0. \\
& \mathbf{r}(t_f) = \mathbf{0},\ \mathbf{v}(t_f) = \mathbf{0}.
\end{aligned}$$

For the optimal guidance of both phases that leads to a fuel-optimal and precise landing, a multi-phase optimal control problem is described below including dynamics and constraints described for each phase and additional constraints to guarantee a smooth transition from one phase to the other.

C. Fuel-Optimal Guidance for End-to-End Human-Mars EDL Mission

When considering the 2D end-to-end EDL mission, the ending point of the entry phase is the starting point of the powered descent phase. Therefore, continuity constraints on position and velocity are imposed on the transition point, expressed as

$$\mathbf{r}(t_I)\cdot\mathbf{e} = (R(t_I)h_0 - R_m)/1000, \tag{12a}$$

$$\mathbf{v}(t_I) = \left[V(t_I)\sqrt{h_0 g_0}\cos\gamma/100, V(t_I)\sqrt{h_0 g_0}\sin\gamma/100\right]^T. \tag{12b}$$

Combining the two guidance problems in (6) and (11) and the continuity constraints, the multi-phase fuel-optimal EDL guidance problem is summarized as

$$\min_{C_L,\mathbf{T},t_I,t_f} \int_{t_I}^{t_f} \dot{m}\, \mathrm{d}t \tag{13}$$

$$\begin{aligned}
\text{subject to } & \dot{R}(t) = V\sin\gamma,\ \forall t \in [t_0, t_I], \\
& \dot{V} = -D - \frac{\sin\gamma}{(Rh_0/R_m)^2}, \\
& \dot{\gamma} = \frac{1}{V}\left(L + V^2\frac{\cos\gamma}{r} - \frac{\cos\gamma}{(Rh_0/R_m)^2}\right), \\
& \dot{\mathbf{r}} = \mathbf{v},\ \dot{\mathbf{v}} = \mathbf{g} + \frac{\mathbf{T}}{m},\ \dot{m} = -\eta\|\mathbf{T}\|_2,\ \forall t \in [t_I, t_f], \\
& C_D = c_{d_0} + c_{d_1}C_L + c_{d_2}C_L^2, \\
& \dot{Q} = k_Q\sqrt{\frac{\rho}{R_{\text{nose}}}}V^{3.15} \le \dot{Q}_{\max}, \\
& \bar{q} = \frac{g_0 m_0 \rho V^2}{2} \le \bar{q}_{\max},
\end{aligned}$$

$$
\begin{aligned}
&\sqrt{L^2+D^2} \le n_{\max},\ \forall t \in [t_0, t_I],\\
&T_{\min} \le \|\mathbf{T}\|_2 \le T_{\min},\ \mathbf{r} \in \mathcal{C},\ \forall t \in [t_I, t_f],\\
&R(t_0) = R_0,\ V(t_0) = V_0,\ \gamma(t_0) = \gamma_0,\\
&R_I^L \le R(t_I) \le R_I^U, \mathbf{r}(t_f) = \mathbf{0},\ \mathbf{v}(t_f) = \mathbf{0},\\
&t_f \le t_{\max},\ m(t_I) = m_{\text{pdi}},\ m(t_f) \ge m_{\text{dry}},\\
&\mathbf{r}(t_I) \cdot \mathbf{e} = (R(t_I)h_0 - R_m)/1000,\\
\mathbf{v}(t_I) = &\left[V(t_I)\sqrt{h_0 g_0}\cos\gamma/100,\ V(t_I)\sqrt{h_0 g_0}\sin\gamma/100\right]^T,
\end{aligned}
$$

where $t_{\max}$ is the maximum duration of the entire EDL mission. By integrating the entry and powered descent phases, the end-to-end EDL guidance problem will determine the transition point between the two phases, as well as the optimal guidance laws and duration for each phase, which provides more flexibility in planning the entire mission.

The end-to-end EDL guidance problem in (13) is a multi-phase nonlinear optimal control problem subject to complicated dynamical and mission constraints. Furthermore, the duration of each phase and transition point between phases are unknown. Solving this nonconvex problem directly is computationally difficult. Therefore, we will first reformulate (13) as a polynomial optimal control problem by approximating all non-polynomial functions, e.g., the atmosphere density model, using continuous polynomials. Then the end-to-end EDL guidance problem will be reformulated as a polynomial programming problem via discretization.

D. Conversion into a Polynomial Optimal Control Problem

In the end-to-end EDL guidance problem formulated in (13), there are several non-polynomial functions, including trigonometric functions, e.g., $\sin\gamma$ and $\cos\gamma$, in the entry phase dynamics, and exponential functions in the heating load constraint and the atmosphere density model. The conversion of these non-polynomials into polynomials using approximate functions is presented below.

1) Mars atmosphere density model: Based on the Mars atmosphere model in [41], the atmosphere model is divided into two zones with different curves, the low altitude atmosphere curve and the high altitude atmosphere curve. The entry phase is defined at a high altitude ranging from 7,000 meters to the boundary of the Mars atmosphere which is at the altitude of 110,000 meters. Then, only the high altitude atmosphere model is considered during the entry phase. For the high altitude atmosphere model, the temperature decreases linearly and the pressure decreases exponentially, expressed as

$$
\rho = \frac{P_{\text{pressure}}}{0.1921\,(T_{\text{temp}} + 273.1)}, \tag{14}
$$

where P_{pressure} and T_{temp} are the atmosphere pressure and temperature, respectively. Moreover, the curve fitting results for P_{pressure} and T_{temp} with respect to the altitude $h = Rh_0 - R_m$ are written as $T_{\text{temp}} = -31\text{–}0.000998h,\ P_{\text{pressure}} = 0.699\exp(-0.00009h)$. Finding a polynomial curve to fit ρ with respect to h according to (14) is straightforward. The classical curve fitting method,

such as the least square method, can find a polynomial function directly. However, using a polynomial to directly fit (14) will result in negative values at some points of the approximate air density function. Thus, (14) is firstly approximated by an exponential function, expressed as

$$\rho = \hat{w}_1 \exp\left(\hat{w}_2 \cdot h\right), \tag{15}$$

where $\hat{w}_1$ and $\hat{w}_2$ denote the curve fitting parameters. Then (15) is further approximated using the Taylor series expansion to fit the exponential function in (15), written as

$$\rho = \hat{w}_1 \sum_{n=0}^{\infty} \frac{(\hat{w}_2 \cdot h)^n}{n!}, \tag{16}$$

In this paper, we use a 6th ($n = 6$) order polynomial function to approximately represent the atmosphere density. The curve fitting result and the residuals are shown in Fig. 1.

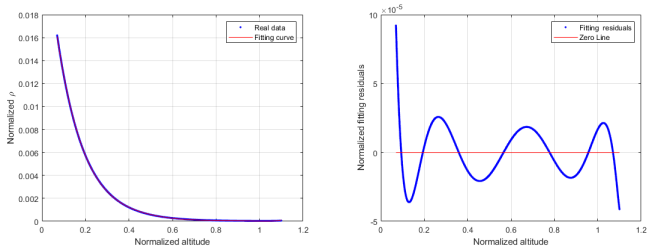

(a) Polynomial approximation for air density (b) Residuals of the fitting curve

Fig. 1: Polynomial curve fitting of the atmosphere density model

2) Heating load constraint: The non-polynomial heating load constraint in (3) can be equivalently rewritten as

$$V \leq \sqrt[3.15]{\frac{\dot{Q}_{\max}}{k_Q \sqrt{\rho / R_{\text{nose}}}}} := V_{\max}. \tag{17}$$

Since ρ is expressed as a function of h in (16), $V_{\max}$ can be approximated as

$$V_{\max}(h) \approx \sum_{i=0}^{n_l} \omega_i h^{n_l}, \tag{18}$$

where $\omega_i, i = 0, 1, \ldots, n_l$, are the coefficients of the fitting polynomial. Let $n_l = 4$ in (18), the approximated results are shown in Fig. 2. Then, the heating rate constraint can be replaced by

$$V \leq \omega_0 + \omega_1 \cdot h + \omega_2 \cdot h^2 + \omega_3 \cdot h^3 + \omega_4 \cdot h^4. \tag{19}$$

3) Normal load constraint: The non-polynomial normal load constraint in (5) can be equivalently reformulated as

$$\sqrt{\left(\frac{1}{2} C_L S \rho V^2\right)^2 + \left(\frac{1}{2} C_D S \rho V^2\right)^2} \leq n_{\max}. \tag{20}$$

By denoting $C_A = \sqrt{C_L^2 + C_D^2}$, the normal load constraint can be replaced by

$$\frac{1}{2} C_A S \rho V^2 \leq n_{\max}. \tag{21}$$

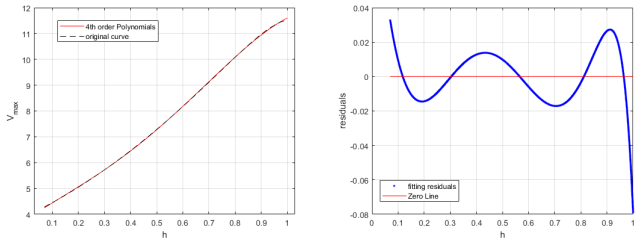

(a) Polynomial fitting for $V_{\max}$ (b) Fitting residuals for $V_{\max}$

Fig. 2: Polynomial fitting results for $V_{\max}$

4) Trigonometric functions in entry phase dynamics: There are nonlinear sinusoidal/cosinusoidal functions of the flight path angle, $\gamma \in [-\frac{\pi}{2}, \frac{\pi}{2}]$, in the entry phase dynamic constraints. Let $a = \sin\gamma$, $b = \cos\gamma$, then $a^2 + b^2 = 1$. As γ is the flight-path angle and $\gamma \in [-\frac{\pi}{2}, \frac{\pi}{2}]$, we have

$$\gamma = \arcsin a,\ \dot{\gamma} = \frac{1}{\sqrt{1-a^2}}\dot{a} = \frac{\dot{a}}{b}, \tag{22}$$

Thus, the dynamic equations in (1) are equivalent to

$$\dot{R} = V \cdot a, \tag{23a}$$

$$\dot{V} = -D - \frac{a}{(Rh_0/R_m)^2}, \tag{23b}$$

$$\dot{a} = \frac{b}{V}\left(L + V^2 \cdot \frac{b}{R} - \frac{b}{(Rh_0/R_m)^2}\right). \tag{23c}$$

With the conversions in (16), (18), and (23), the EDL guidance problem in (13) can be reformulated as a polynomial optimal control problem. Via discretization, a polynomial optimal control problem can be converted into a polynomial programming problem. By introducing extra variables and quadratic constraints, every polynomial programming problem can be expressed as an equivalent nonconvex QCQP [29]. The discretization and conversion steps are detailed below.

E. Discretization and Conversion into QCQP

We first discretize the trajectories in the entry phase and powered descent phase into $N_1 > 0$ and $N_2 > 0$ intervals, respectively, shown in Fig. 3. The equations of motion of the entry phase are then approximated by the Euler integration scheme, expressed as

$$\frac{R_{i+1} - R_i}{\Delta t_1} = V_i a_i, \tag{24a}$$

$$\frac{V_{i+1} - V_i}{\Delta t_1} = -\frac{1}{2}C_{D_i} S \rho_i V_i^2 - \frac{a_i}{(R_i h_0/R_m)^2}, \tag{24b}$$

$$\frac{a_{i+1} - a_i}{\Delta t_1} = \frac{b_i}{V_i}\left(\frac{1}{2}C_{L_i} S \rho_i V_i^2 + \frac{V_i^2 b_i}{R_i} - \frac{b_i}{(R_i h_0/R_m)^2}\right),$$

$$i = 1, 2, ..., N_1 \tag{24c}$$

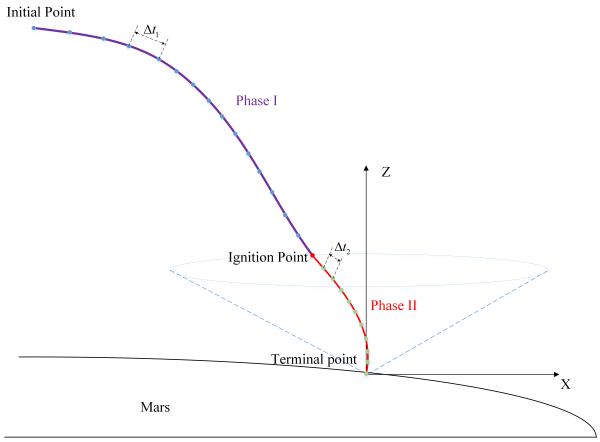

Fig. 3: Discretized trajectory of multi-phase human-Mars EDL

where $\Delta t_1 = (t_I - t_0)/N_1$ is the uniform time step between two adjacent discrete nodes for the entry phase. Next, we denote

$$\begin{aligned}
&\delta R_i = \frac{R_{i+1} - R_i}{\Delta t_1},\ \delta V_i = \frac{V_{i+1} - V_i}{\Delta t_1},\ \delta p_i = \frac{p_i}{\Delta t_1},\\
&p_i = \frac{(a_{i+1} - a_i)\cdot V_i}{b_i}, \hat{V}_i = V_i^2,\ \hat{h}_i = h_i^2,\ \tilde{h}_i = h_i^3 = h_i \cdot \hat{h}_i,\\
&\bar{h}_i = h_i^4 = \hat{h}_i^2, \grave{h}_i = h_i^5 = \tilde{h}_i \cdot \hat{h}_i,\ \check{h}_i = h_i^6 = \tilde{h}_i^2,\\
&l_i = \frac{a_i}{\hat{h}_i + 2h_i R_m/h_0 + (R_m/h_0)^2},\ h_i = R_i - \frac{R_m}{h_0},\\
&f_i = \hat{V}_i - \frac{1}{R_i(h_0/R_m)^2},\ e_i = \frac{b_i \cdot f_i}{R_i},\\
&q_i = \hat{V}_i\rho = \hat{V}_i\hat{w}_1\left(1 + \hat{w}_2 \cdot h_i + \frac{\hat{w}_2^2 \cdot \hat{h}_i}{2} + \frac{\hat{w}_2^3 \cdot \tilde{h}_i}{6}\right)\\
&\qquad + \hat{V}_i\hat{w}_1\left(\frac{\hat{w}_2^4 \cdot \bar{h}_i}{24} + \frac{\hat{w}_2^5 \cdot \grave{h}_i}{120} + \frac{\hat{w}_2^6 \cdot \check{h}_i}{720}\right)
\end{aligned} \tag{25a}$$

Using the above intermediate variables, (24) can be rewritten as quadratic constraints, expressed as

$$\delta R_i = V_i a_i \tag{26a}$$

$$\delta V_i = -\left(\frac{S}{2} C_{D_i} q_i + l_i\right) \tag{26b}$$

$$\delta p_i = \frac{S}{2} C_{L_i} q_i + e_i \tag{26c}$$

Meanwhile, the mission constraints in (3)-(5) at every discrete node, $i = 1, \ldots, N_1$, for the entry phase can also be rewritten as quadratic inequalities, expressed as

$$V_i \le \omega_0 + \omega_1 h_i + \omega_2 \hat{h}_i + \omega_3 \tilde{h}_i + \omega_4 \bar{h}_i, \tag{27a}$$

$$q_i \le \frac{2\bar{q}_{\max}}{m_0 g_0}, \tag{27b}$$

$$\frac{1}{2} C_{A_i} S q_i \le n_{\max},\ C_{A_i}^2 = C_{L_i}^2 + C_{D_i}^2. \tag{27c}$$

Applying the Euler integration rule to the equations of motion in (7) during the powered descent phase, leads to

$$\frac{x_{j+1}-x_j}{\Delta t_2}=v_{x_j},\quad \frac{z_{j+1}-z_j}{\Delta t_2}=v_{z_j}, \tag{28a}$$

$$\frac{v_{x_{j+1}}-v_{x_j}}{\Delta t_2}=\frac{T_{x_j}}{m_j},\quad \frac{v_{z_{j+1}}-v_{z_j}}{\Delta t_2}=\frac{T_{z_j}}{m_j}-g_0, \tag{28b}$$

$$\frac{m_{j+1}-m_j}{\Delta t_2}=-\eta T_i,\quad T_j^2=T_{x_j}^2+T_{z_j}^2,\ j=1,...,N_2, \tag{28c}$$

where $\Delta t_2=(t_f-t_I)/N_2$ and T_i is the magnitude of thrust vector $\mathbf{T}$. Since t_I and t_f are unknown, Δt_1 and Δt_2 are to be determined in the EDL guidance problem. Through above conversions, all dynamics and mission constraints are reformulated as linear or quadratic equalities/inequalities for both phases. By denoting

$$\begin{aligned}\mathbf{X}=[&R,h,\hat{h},\tilde{h},\bar{h},\grave{h},\check{h},\delta R,V,\hat{V},\delta V,a,b,e,f,p,\delta p,l,q,\\&C_A,C_L,C_D,x,v_x,z,v_z,m,T_x,T_z,T,\Delta t_1,\Delta t_2]^T,\end{aligned}$$

the original EDL guidance problem in (13) is now cast as a QCQP, summarized as

$$\begin{aligned}\min_{\mathbf{X}}\quad & -m_{N_2} \\ \text{subject to}\quad & (25)\ \&\ (26),\\ & (28),\\ & V_i\le\omega_0+\omega_1h_i+\omega_2\hat{h}_i+\omega_3\tilde{h}_i+\omega_4\bar{h}_i,\\ & q_i\le\frac{2\bar{q}_{\max}}{m_0g_0},\\ & \frac{1}{2}C_{A_i}Sq_i\le n_{\max},\\ & C_{A_i}^2=C_{D_i}^2+C_{L_i}^2,\\ & C_{D_i}=c_{d_0}+c_{d_1}C_{L_i}+c_{d_2}C_{L_i}^2,\\ & T_{\min}\le T_j\le T_{\max},\\ & z_j^2\ge x_j^2\cdot\cot^2(\theta),\\ & R_1=R_0,\ V_1=V_0,\\ & R_I^L\le R_{N_1}\le R_I^U,\\ & x_{N_2}=z_{N_2}=0,\ v_{x_{N_2}}=v_{z_{N_2}}=0,\\ & [x_1,z_1]\cdot\mathbf{e}=(R_{N_1}h_0-R_m)/1000,\\ [v_{x_1},v_{z_1}]=&[V_{N_1}b_{N_1}\sqrt{h_0g_0}/100,V_{N_1}a_{N_1}\sqrt{h_0g_0}/100]^T,\end{aligned} \tag{29}$$

where $i=1,\dots,N_1$ and $j=1,\dots,N_2$.

II. A Customized ADMM for Nonconvex QCQPs

A. Customized ADMM Framework

Since a general QCQP can be equivalently formulated as a homogeneous QCQP, we focus on solving the homogeneous QCQP formulated as

$$\begin{aligned} &\min_{\mathbf{x}\in\mathbb{R}^n} \mathbf{x}^T\mathbf{Q}_0\mathbf{x} \\ &\text{subject to } \mathbf{x}^T\mathbf{Q}_i\mathbf{x} = c_i,\ i\in\mathcal{E} \\ &\qquad \mathbf{x}^T\mathbf{P}_j\mathbf{x} \le d_j,\ j\in\mathcal{I} \end{aligned} \tag{30}$$

where $\mathbf{x}\in\mathbb{R}^n$ is the unknown vector to be determined, $\mathbf{Q}_0\in\mathbb{R}^{n\times n}$, $\mathbf{Q}_i\in\mathbb{R}^{n\times n}$, $i\in\mathcal{E}$, and $\mathbf{P}_j\in\mathbb{R}^{n\times n}$, $j\in\mathcal{I}$ are real symmetric matrices which are not necessarily positive semidefinite. $\mathcal{E}$ and $\mathcal{I}$ are the indices sets of equality and inequality constraints, respectively. Due to the indefiniteness of $\mathbf{Q}_i$ or $\mathbf{P}_j$, problem (30) is generally nonconvex and NP-hard. In order to solve the nonconvex QCQP, we equivalently transform (30) into a consensus-constrained optimization problem formulated as

$$\begin{aligned} &\min_{\mathbf{x},\mathbf{y}} \mathbf{x}^T\mathbf{Q}_0\mathbf{y} \\ &\text{subjecto to } \mathbf{x}^T\mathbf{Q}_i\mathbf{y} = c_i, i\in\mathcal{E} \\ &\qquad \mathbf{x}^T\mathbf{P}_j\mathbf{y} \le d_j, j\in\mathcal{I} \\ &\qquad \mathbf{x} = \mathbf{y}. \end{aligned} \tag{31}$$

Obviously, with the consensus constraint $\mathbf{x}=\mathbf{y}$, problems (30) and (31) are equivalent. Let $\boldsymbol{\nu}\in\mathbb{R}^n$, $\boldsymbol{\mu}\in\mathbb{R}^{|\mathcal{E}|}$, $\boldsymbol{\lambda}\in\mathbb{R}^{|\mathcal{I}|}$ be the Lagrange multipliers associated with the consensus constraint, equality constraints, and inequality constraints in (31), respectively. For notational convenience, we denote $\Lambda = \left[\boldsymbol{\nu}^T, \boldsymbol{\mu}^T, \boldsymbol{\lambda}^T\right]^T$. Typically, the inequality constraints are converted into equalities by introducing slack variables. Without using the slack variables, switching functions are applied to reformulate the inequality constraints, expressed as

$$\begin{aligned} f_\zeta(s,q) &= \frac{1}{2\zeta}\left(\max\{0, s+\zeta q\}^2 - s^2\right) \\ &= \begin{cases} -\frac{s^2}{2\zeta}, & s+\zeta q \le 0 \\ \frac{2sq+q^2\zeta}{2}, & s+\zeta q \ge 0 \end{cases} \end{aligned} \tag{32}$$

where the right side in (32) are component-wise operations when s and q are vectors. By utilizing (32) to handle the inequalities in (31), the augmented Lagrangian for (31) can be written as

$$\begin{aligned} &\mathcal{L}_{\mathbf{p}}(\mathbf{x},\mathbf{y},\Lambda) = \mathbf{x}^T\mathbf{Q}_0\mathbf{y} + \boldsymbol{\nu}^T(\mathbf{x}-\mathbf{y}) + \frac{\zeta_1}{2}\|\mathbf{x}-\mathbf{y}\|^2 \\ &+ \sum_{i\in\mathcal{E}}\left(\mu_i\left(\mathbf{x}^T\mathbf{Q}_i\mathbf{y} - c_i\right) + \frac{\zeta_2}{2}\left\|\mathbf{x}^T\mathbf{Q}_i\mathbf{y} - c_i\right\|^2\right) \\ &+ \sum_{j\in\mathcal{I}} f_{\zeta_3}\left(\lambda_j, \mathbf{x}^T\mathbf{P}_j\mathbf{y} - d_j\right), \end{aligned} \tag{33}$$

where $\mathbf{p} = [\zeta_1, \zeta_2, \zeta_3]$ is the collection of the penalty coefficients associated with the augmented terms. By employing the classical ADMM framework [42], [43] to solve (31), the variables $\mathbf{x}$, $\mathbf{y}$ and the Lagrange multipliers Λ at step $(k+1)$ can be updated as follows:

$$\mathbf{x}^{k+1} = \arg\min_{\mathbf{x}} \mathcal{L}_{\mathbf{p}^k}(\mathbf{x}, \mathbf{y}^k, \Lambda^k) \tag{34a}$$

$$\mathbf{y}^{k+1} = \arg\min_{\mathbf{y}} \mathcal{L}_{\mathbf{p}^k}(\mathbf{x}^{k+1}, \mathbf{y}, \Lambda^k) \tag{34b}$$

$$\boldsymbol{\nu}^{k+1} = \boldsymbol{\nu}^k + \zeta_1^k \left(\mathbf{x}^{k+1} - \mathbf{y}^{k+1}\right) \tag{34c}$$

$$\mu_i^{k+1} = \mu_i^k + \zeta_2^k \left((\mathbf{x}^{k+1})^T \mathbf{Q}_i \mathbf{y}^{k+1} - c_i\right), \ \forall i \in \mathcal{E} \tag{34d}$$

$$\lambda_j^{k+1} = \max\{0, \lambda_j^k + \zeta_3^k \left((\mathbf{x}^{k+1})^T \mathbf{P}_j \mathbf{y}^{k+1} - d_j\right)\}, \forall j \in \mathcal{I} \tag{34e}$$

where each penalty coefficient in $\mathbf{p}^k$ are chosen as a non-decreasing positive sequence. Specifically, they are determined according to the following updating rules,

$$\zeta_1^{k+1} = \begin{cases} \beta\zeta_1^k, & \text{if } \|\mathbf{x}^{k+1} - \mathbf{y}^{k+1}\| \geq \tau\|\mathbf{x}^k - \mathbf{y}^k\| \\ \zeta_1^k, & \text{otherwise} \end{cases} \tag{35a}$$

$$\zeta_2^{k+1} = \begin{cases} \beta\zeta_2^k, & \text{if } \|(\mathbf{x}^{k+1})^T \mathbf{Q}_i \mathbf{y}^{k+1} - c_i\| \\ & \geq \tau\|(\mathbf{x}^k)^T \mathbf{Q}_i \mathbf{y}^k - c_i\| \\ \zeta_2^k, & \text{otherwise} \end{cases} \tag{35b}$$

$$\zeta_3^{k+1} = \begin{cases} \beta\zeta_3^k, & \text{if } \|[(\mathbf{x}^{k+1})^T \mathbf{P}_j \mathbf{y}^{k+1} - d_j]^+\| \\ & \geq \tau\|[(\mathbf{x}^k)^T \mathbf{P}_j \mathbf{y}^k - d_j]^+\| \\ \zeta_3^k, & \text{otherwise} \end{cases} \tag{35c}$$

where

$$\begin{aligned} &\left[(\mathbf{x}^{k+1})^T \mathbf{P}_j \mathbf{y}^{k+1} - d_j\right]^+ \\ &\qquad := \max\left\{(\mathbf{x}^{k+1})^T \mathbf{P}_j \mathbf{y}^{k+1} - d_j, -\lambda_j^{k+1}/\zeta_3^k\right\}, \end{aligned}$$

$\beta \geq 1$ and τ are positive constants. The updates of Lagrange multipliers in (34) are straightforward. However, the updates of $\mathbf{x}$ and $\mathbf{y}$ require to solve two sequences of convex quadratic optimization problems. Specifically, for the $\mathbf{x}$-update, (33) is a ζ_1^k-strongly convex function when $\mathbf{y} = \mathbf{y}^k$ and $\Lambda = \Lambda^k$ are given. Thus, the global optimum of the sequential subproblem (34a) can be derived from the first order optimality conditions of (33), written as

$$\begin{aligned} &\frac{\partial \mathcal{L}_{\mathbf{p}^k}(\mathbf{x}, \mathbf{y}^k, \Lambda^k)}{\partial \mathbf{x}} = \mathbf{Q}_0 \mathbf{y}^k + \boldsymbol{\nu}^k + \zeta_1^k \left(\mathbf{x} - \mathbf{y}^k\right) \\ &\sum_{i \in \mathcal{E}} \left(\mu_i^k \mathbf{Q}_i \mathbf{y}^k + \zeta_2^k \left(\mathbf{x}^T \mathbf{Q}_i \mathbf{y}^k - c_i\right) \mathbf{Q}_i \mathbf{y}^k\right) \\ &+ \sum_{j \in \mathcal{I}} \Gamma_{xj}^k \left(\lambda_j^k \mathbf{P}_j \mathbf{y}^k + \zeta_3^k \left(\mathbf{x}^T \mathbf{P}_j \mathbf{y}^k - d_j\right) \mathbf{P}_j \mathbf{y}^k\right) \\ &= \mathbf{0}, \end{aligned} \tag{36}$$

where ${\Gamma_{xj}}^k$, $j \in \mathcal{I}$, is a logical function associated with the inequality constraint j at kth step, which is defined as

$$\Gamma_{xj}^k = \begin{cases} 0, & \lambda_j^k + \zeta_3^k \left((\mathbf{x}^k)^T \mathbf{P}_j \mathbf{y}^k - d_j \right) \leq 0, \\ 1, & \lambda_j^k + \zeta_3^k \left((\mathbf{x}^k)^T \mathbf{P}_j \mathbf{y}^k - d_j \right) > 0. \end{cases} \tag{37}$$

By solving (36), we can find the closed-form solution of the $\mathbf{x}$-update, expressed as

$$\mathbf{x}^{k+1} = \left(\mathbf{A}_x^k \right)^{-1} \mathbf{b}_x^k, \tag{38}$$

where $\mathbf{A}_x^k$ and $\mathbf{b}_x^k$ are defined as

$$\begin{aligned} \mathbf{A}_x^k = & \zeta_1^k \mathbf{I} + \sum_{i \in \mathcal{E}} \zeta_2^k \left(\mathbf{Q}_i \mathbf{y}^k \right) \left(\mathbf{Q}_i \mathbf{y}^k \right)^T \\ & + \sum_{j \in \mathcal{I}} \Gamma_{xj}^k \zeta_3^k \left(\mathbf{P}_j \mathbf{y}^k \right) \left(\mathbf{P}_j \mathbf{y}^k \right)^T, \end{aligned} \tag{39a}$$

$$\begin{aligned} \mathbf{b}_x^k = & -\mathbf{Q}_0 \mathbf{y}^k - \boldsymbol{\nu}^k + \zeta_1^k \mathbf{y}^k - \sum_{i \in \mathcal{E}} \left(\left(\mu_i^k - \zeta_2^k c_i \right) \mathbf{Q}_i \mathbf{y}^k \right) \\ & - \sum_{j \in \mathcal{I}} \left(\Gamma_{xj}^k \left(\lambda_j^k - \zeta_3^k d_i \right) \mathbf{P}_j \mathbf{y}^k \right), \end{aligned} \tag{39b}$$

where $\mathbf{A}_{\mathbf{x}}^k$ is a positive definite matrix when the elements in $\mathbf{p}^k$ are all positive. Similarly, with the given $\mathbf{x}^{k+1}$ and Λ^k, the closed-form solution of the sequential subproblem (34b) for $\mathbf{y}$-update can be obtained from

$$\mathbf{y}^{k+1} = \left(\mathbf{A}_y^k \right)^{-1} \mathbf{b}_y^k, \tag{40}$$

where

$$\begin{aligned} \mathbf{A}_y^k = & \zeta_1^k \mathbf{I} + \sum_{i \in \mathcal{E}} \zeta_2^k \left(\mathbf{Q}_i \mathbf{x}^{k+1} \right) \left(\mathbf{Q}_i \mathbf{x}^{k+1} \right)^T \\ & + \sum_{j \in \mathcal{I}} \Gamma_{yj}^k \zeta_3^k \left(\mathbf{P}_j \mathbf{x}^{k+1} \right) \left(\mathbf{P}_j \mathbf{x}^{k+1} \right)^T, \end{aligned} \tag{41a}$$

$$\begin{aligned} \mathbf{b}_y^k = & -\mathbf{Q}_0 \mathbf{x}^{k+1} + \boldsymbol{\nu}^k + \zeta_1^k \mathbf{x}^{k+1} \\ & - \sum_{i \in \mathcal{E}} \left(\left(\mu_i^k - \zeta_2^k c_i \right) \mathbf{Q}_i \mathbf{x}^{k+1} \right) \\ & - \sum_{j \in \mathcal{I}} \left(\Gamma_{yj}^k \left(\lambda_j^k - \zeta_3^k d_j \right) \mathbf{P}_j \mathbf{x}^{k+1} \right), \end{aligned} \tag{41b}$$

$$\Gamma_{yj}^k = \begin{cases} 0, & \lambda_j^k + \zeta_3^k \left((\mathbf{x}^{k+1})^T \mathbf{P}_j \mathbf{y}^k - d_j \right) \leq 0; \\ 1, & \lambda_j^k + \zeta_3^k \left((\mathbf{x}^{k+1})^T \mathbf{P}_j \mathbf{y}^k - d_j \right) > 0. \end{cases} \tag{41c}$$

With the analytical solutions in (38) and (40) derived for subproblems (34a) and (34b), the customized ADMM for nonconvex QCQPs in (30) is summarized in Algorithm 1.

Algorithm 1 Customized ADMM for nonconvex QCQP in (30)

Input: $\mathbf{Q}_0$, $\mathbf{Q}_i$, $\mathbf{c}_i$, $i \in \mathcal{E}$, $\mathbf{P}_j$, $\mathbf{d}_j$, $j \in \mathcal{I}$, and constant parameters β, τ, ϵ
Output: Unknown vectors $\mathbf{x}$ and $\mathbf{y}$
Initialization: $\mathbf{x}^0, \mathbf{y}^0, \Lambda^0$ and penalty coefficients $\mathbf{p}^0$

```
for k = 0, 1, 2, ... do
    Calculate the logical function Γ_{x_j}^k with x^k, y^k, Λ^k;
    x^{k+1}-update using (38) with y^k, Λ^k;
    Calculate the logical function Γ_{y_j}^k with x^{k+1}, y^k, Λ^k;
    y^{k+1}-update using (40) with x^{k+1}, Λ^k;
    Update Lagrange multipliers Λ using (34c), (34d), and (34e) with x^{k+1} and y^{k+1};
    Penalty coefficients updates using (35);
    Calculate the error vector ξ = [ ||x^{k+1} − y^{k+1}|| / ||x^{k+1}||, Σ_{i∈E} ||(x^{k+1})^T Q_i y^{k+1} − c|| / ||c||, Σ_{j∈I} (||Γ_{x_j}^k|| + ||Γ_{y_j}^k||) / 2 ]
    if ||ξ||_1 ≤ ε then
        break;
    end if
    k = k + 1
end for
```

B. Convergence Analysis of ADMM

Assumption II.1. *In problem* (30)*, the objective function and constraints are of class* $\mathcal{C}^2$*. Problem* (30) *has at least one feasible solution and the objective function is lower bounded.*

Assumption II.2. *The coefficient matrices* $\mathbf{Q}_1, \mathbf{Q}_2, \cdots, \mathbf{Q}_{|\mathcal{E}|}$ *of all equality constraints in a QCQP satisfy that for any vector* $\mathbf{x} \in \mathbb{R}^n$ *without zero entries, the row vectors of* $[(\mathbf{x})^T\mathbf{Q}_1; (\mathbf{x})^T\mathbf{Q}_2; \ldots; (\mathbf{x})^T\mathbf{Q}_k] \in \mathbb{R}^{k\times n}$ *are linearly independent, where* $|\mathcal{E}|$ *denotes the cardinality of* $\mathcal{E}$*. Moreover, the coefficient matrices of all inequality constraints* $\mathbf{P}_1, \mathbf{P}_2, \ldots, \mathbf{P}_{|\mathcal{I}|}$ *also satisfy that the row vectors of* $[(\mathbf{x})^T\mathbf{P}_1; (\mathbf{x})^T\mathbf{P}_2; \ldots; (\mathbf{x})^T\mathbf{P}_k] \in \mathbb{R}^{k\times n}$ *are linearly independent, where* $|\mathcal{I}|$ *is the cardinality of* $\mathcal{I}$*.*

Denote

$$\mathbf{Q}_{\mathcal{E}}\mathbf{x} = \left[(\mathbf{x})^T\mathbf{Q}_1, (\mathbf{x})^T\mathbf{Q}_2, \cdots, (\mathbf{x})^T\mathbf{Q}_{|\mathcal{E}|}\right] \in \mathbb{R}^{|\mathcal{E}|\times n},$$

where $\mathbf{Q}_{\mathcal{E}}\mathbf{x}$ has a full column rank. As a result, $\sigma_{\min}(\mathbf{Q}_{\mathcal{E}}\mathbf{x}) > 0$, where $\sigma_{\min}(\bullet)$ denotes the minimum singular value of '$\bullet$'. Then, for any vector $\boldsymbol{\mu} \in \mathbb{R}^{|\mathcal{E}|}$, we have

$$\left\|(\mathbf{Q}_{\mathcal{E}}\mathbf{x})^T\boldsymbol{\mu}\right\| \geq \sigma_{\min}(\mathbf{Q}_{\mathcal{E}}\mathbf{x})\|\boldsymbol{\mu}\|. \tag{42}$$

Similarly, for the inequality constraints, we have $\mathbf{P}_{\mathcal{I}}\mathbf{x} = \left[(\mathbf{x})^T\mathbf{P}_1, (\mathbf{x})^T\mathbf{P}_2, \cdots, (\mathbf{x})^T\mathbf{P}_{|\mathcal{I}|}\right] \in \mathbb{R}^{|\mathcal{I}|\times n}$ has a full column rank and $\sigma_{\min}(\mathbf{P}_{\mathcal{I}}\mathbf{x}) > 0$.

In the end-to-end EDL guidance problem formulated in (29), it is obvious that the objective and constraints in (29) are all of class $\mathcal{C}^2$, and the objective function is lower bounded, which indicates that Assumption II.1 is valid for (29). Moreover, each equality constraint associated with the discretized dynamics only include the state and control variables at current discrete node and/or its adjacent nodes. As a result, the vectors $\mathbf{Q}_i\mathbf{x}$ are linearly independent. A similar observation could be found for the inequality constraints. Therefore, assumption II.2 is valid for the formulated Mars EDL problem in (29).

Note that, when Assumption II.2 holds and $\mathbf{x}^k$ is given, the equality constraints of (31), i.e., $(\mathbf{x}^k)^T\mathbf{Q}_i\mathbf{y} - c_i = 0$, will be linearly independent with respect to $\mathbf{y}$. In addition, in the formulated QCQP in (29), each equality constraint involves different state and control variables at each discrete node, which leads to the linear independence of the vectors $\mathbf{Q}_1\mathbf{x}, \mathbf{Q}_2\mathbf{x}, \cdots, \mathbf{Q}_{|\mathcal{E}|}\mathbf{x}$.

Definition II.3. ***Strong convexity****: A function f is called κ-strongly convex if there exists a positive constant κ such that the following condition holds for all points x, y in its domain:*

$$f(y) \geq f(x) + \bigtriangledown f(x)^T(y-x) + \frac{\kappa}{2}\|y-x\|^2. \tag{43}$$

Moreover, if the function $f \in \mathcal{C}^2$, then it is κ-strongly convex if and only if $\bigtriangledown^2 f(x) \succeq \kappa\mathbf{I}$ for all x in the domain, where $\mathbf{I}$ is the identity matrix and $\bigtriangledown^2 f$ is the Hessian matrix, and the symbol '$\succeq$' means that $\bigtriangledown^2 f(x) - \kappa\mathbf{I}$ is positive semi-definite.

Lemma II.4. *At every iteration, the $\mathbf{x}^k$-update in sub-problem* (34a) *and $\mathbf{y}^k$-update in sub-problem* (34b)*, $k = 1, 2, \ldots$, are feasible and strongly convex.*

Proof. At every iteration, for the $\mathbf{x}$-update and $\mathbf{y}$-update, the Hessian matrices of the Lagrangian are expressed as

$$\begin{aligned}\bigtriangledown^2_{\mathbf{x}}\mathcal{L} =& \zeta_1\mathbf{I} + \sum_{i\in\mathcal{E}} \zeta_2 \left(\mathbf{Q}_i\mathbf{y}\right)\left(\mathbf{Q}_i\mathbf{y}\right)^T \\ &+ \zeta_3 \sum_{j\in\mathcal{I}} \Gamma_{xj} \left(\mathbf{P}_j\mathbf{y}\right)\left(\mathbf{P}_j\mathbf{y}\right)^T, \end{aligned} \tag{44a}$$

$$\begin{aligned}\bigtriangledown^2_{\mathbf{y}}\mathcal{L} =& \zeta_1\mathbf{I} + \sum_{i\in\mathcal{E}} \zeta_2 \left(\mathbf{Q}_i\mathbf{x}\right)\left(\mathbf{Q}_i\mathbf{x}\right)^T \\ &+ \zeta_3 \sum_{j\in\mathcal{I}} \Gamma_{yj} \left(\mathbf{P}_j\mathbf{x}\right)\left(\mathbf{P}_j\mathbf{x}\right)^T, \end{aligned} \tag{44b}$$

where k is omitted for notational clarity. With $[\zeta_1, \zeta_2, \zeta_3]$ being positive scalars, there exist $\kappa_x > 0$ and $\kappa_y > 0$ such that $\bigtriangledown^2_{\mathbf{x}}\mathcal{L} \succeq \kappa_x\mathbf{I} \succeq \zeta_1\mathbf{I}$ and $\bigtriangledown^2_{\mathbf{y}}\mathcal{L} \succeq \kappa_y\mathbf{I} \succeq \zeta_1\mathbf{I}$ hold for all $\mathbf{x}, \mathbf{y} \in \mathbb{R}^n$. Meanwhile, the positive definiteness of $\mathbf{A}^k_x$ and $\mathbf{A}^k_y$ makes these subproblems feasible for all k. □

Denoting

$$\begin{aligned}\mathcal{G}(\mathbf{x}, \mathbf{y}, \boldsymbol{\mu}, \boldsymbol{\lambda}) =& \mathbf{x}^T\mathbf{Q}_0\mathbf{y} \\ &+ \sum_{i\in\mathcal{E}} \left(\mu_i\left(\mathbf{x}^T\mathbf{Q}_i\mathbf{y} - c_i\right) + \frac{\zeta_2}{2}\|\mathbf{x}^T\mathbf{Q}_i\mathbf{y} - c_i\|^2\right) \\ &+ \sum_{j\in\mathcal{I}} f_{\zeta_3}\left(\lambda_j, \mathbf{x}^T\mathbf{P}_j\mathbf{y} - d_j\right),\end{aligned}$$

then we have

$$\mathcal{L} = \mathcal{G} + \boldsymbol{\nu}^T\left(\mathbf{x} - \mathbf{y}\right) + \frac{\zeta_1}{2}\|\mathbf{x} - \mathbf{y}\|^2 \tag{45a}$$

$$\bigtriangledown_{\mathbf{x}}\mathcal{L} = \bigtriangledown_{\mathbf{x}}\mathcal{G} + \boldsymbol{\nu} + \zeta_1\left(\mathbf{x} - \mathbf{y}\right) \tag{45b}$$

$$\bigtriangledown^2_{\mathbf{x}}\mathcal{L} = \bigtriangledown^2_{\mathbf{x}}\mathcal{G} + \zeta_1\mathbf{I} \tag{45c}$$

Similarly, by denoting

$$\mathcal{F}(\mathbf{x},\mathbf{y},\boldsymbol{\nu},\boldsymbol{\lambda}) = \mathbf{x}^T\mathbf{Q}_0\mathbf{y} + \boldsymbol{\nu}^T(\mathbf{x}-\mathbf{y}) + \sum_{j\in\mathcal{I}} f_{\zeta_3}\left(\lambda_j, \mathbf{x}^T\mathbf{P}_j\mathbf{y} - d_j\right),$$

we have

$$\mathcal{L} = \mathcal{F} + \boldsymbol{\mu}^T\left(\mathbf{x}^T\mathbf{Q}_{\mathcal{E}}\mathbf{y} - \mathbf{c}\right) + \frac{\zeta_2}{2}\left\|\mathbf{x}^T\mathbf{Q}_{\mathcal{E}}\mathbf{y} - \mathbf{c}\right\|^2, \tag{46a}$$

$$\bigtriangledown_{\mathbf{y}}\mathcal{L} = \bigtriangledown_{\mathbf{y}}\mathcal{F} + \boldsymbol{\mu}^T\mathbf{Q}_{\mathcal{E}}\mathbf{x} + \zeta_2\left(\mathbf{x}^T\mathbf{Q}_{\mathcal{E}}\mathbf{y} - \mathbf{c}\right)\mathbf{Q}_{\mathcal{E}}\mathbf{x}, \tag{46b}$$

$$\bigtriangledown^2_{\mathbf{y}}\mathcal{L} = \bigtriangledown^2_{\mathbf{y}}\mathcal{F} + \zeta_2\left(\mathbf{Q}_{\mathcal{E}}\mathbf{x}\right)^T\left(\mathbf{Q}_{\mathcal{E}}\mathbf{x}\right). \tag{46c}$$

where

$$\mathbf{x}^T\mathbf{Q}_{\mathcal{E}}\mathbf{y} - \mathbf{c} = \begin{bmatrix} \mathbf{x}^T\mathbf{Q}_1\mathbf{y} - c_1 \\ \mathbf{x}^T\mathbf{Q}_2\mathbf{y} - c_2 \\ \vdots \\ \mathbf{x}^T\mathbf{Q}_{|\mathcal{E}|}\mathbf{y} - c_{|\mathcal{E}|} \end{bmatrix} \in \mathbb{R}^{|\mathcal{E}|\times 1}, \tag{47}$$

By denoting

$$\mathcal{H}(\mathbf{x},\mathbf{y},\boldsymbol{\nu},\boldsymbol{\mu}) = \mathbf{x}^T\mathbf{Q}_0\mathbf{y} + \boldsymbol{\nu}^T(\mathbf{x}-\mathbf{y}) + \boldsymbol{\mu}^T\left(\mathbf{x}^T\mathbf{Q}_{\mathcal{E}}\mathbf{y} - \mathbf{c}\right) + \frac{\zeta_2}{2}\left\|\mathbf{x}^T\mathbf{Q}_{\mathcal{E}}\mathbf{y} - \mathbf{c}\right\|^2,$$

we have

$$\mathcal{L} = \mathcal{H} + \sum_{j\in\mathcal{I}} f_{\zeta_3}\left(\lambda_j, \mathbf{x}^T\mathbf{P}_j\mathbf{y} - d_j\right), \tag{48a}$$

$$\bigtriangledown_{\mathbf{y}}\mathcal{L} = \bigtriangledown_{\mathbf{y}}\mathcal{H} + \left(\boldsymbol{\Gamma}_{\boldsymbol{y}}\circ\boldsymbol{\lambda}\right)^T\mathbf{P}_{\mathcal{I}}\mathbf{x} + \zeta_3\boldsymbol{\Gamma}_{\boldsymbol{y}}\circ\left(\mathbf{x}^T\mathbf{P}_{\mathcal{I}}\mathbf{y} - \mathbf{d}\right)\mathbf{P}_{\mathcal{I}}\mathbf{x}, \tag{48b}$$

$$\bigtriangledown^2_{\mathbf{y}}\mathcal{L} = \bigtriangledown^2_{\mathbf{y}}\mathcal{H} + \boldsymbol{\Gamma}_{\boldsymbol{y}}\circ\zeta_3\left(\mathbf{P}_{\mathcal{I}}\mathbf{x}\right)\left(\mathbf{P}_{\mathcal{I}}\mathbf{x}\right)^T. \tag{48c}$$

where $\circ$ denotes the element-wise product.

Lemma II.5. *When Assumption II.1 holds, $\mathcal{G}(\mathbf{x},\mathbf{y},\boldsymbol{\mu},\boldsymbol{\lambda})$, $\mathcal{F}(\mathbf{x},\mathbf{y},\boldsymbol{\nu},\boldsymbol{\lambda})$ and $\mathcal{H}(\mathbf{x},\mathbf{y},\boldsymbol{\nu},\boldsymbol{\mu})$ have Lipschitz continuous gradients with respect to $\mathbf{y}$ for $\zeta_1 > 0, \zeta_2 > 0$ and $\zeta_3 > 0$, respectively.*

Proof. From Assumption II.1, $\mathcal{G} \in \mathcal{C}^2$ is in the set $\left\{(\mathbf{x},\mathbf{y})\,|\mathbf{x}^T\mathbf{P}_j\mathbf{y} - d_j \neq 0, j\in\mathcal{I}\right\}$ for all Λ. Thus, $\bigtriangledown_{\mathbf{y}}\mathcal{G}(\mathbf{x},\mathbf{y},\boldsymbol{\mu},\boldsymbol{\lambda})$ is almost everywhere differentiable. Consider the Hessian matrix of $\mathcal{G}$ with respect to $\mathbf{y}$,

$$\bigtriangledown^2_{\mathbf{y}}\mathcal{G} = \zeta_2\sum_{i\in\mathcal{E}}\left(\mathbf{Q}_i\mathbf{x}\right)\left(\mathbf{Q}_i\mathbf{x}\right)^T + \zeta_3\sum_{j\in\mathcal{I}}\Gamma_{yj}\left(\mathbf{P}_j\mathbf{x}\right)\left(\mathbf{P}_j\mathbf{x}\right)^T. \tag{49}$$

Obviously, $\bigtriangledown^2_{\mathbf{y}}\mathcal{G}$ is positive definite given $\mathbf{x}$ such that $\sum\limits_{i\in\mathcal{E}}\left(\mathbf{Q}_i\mathbf{x}\right)\left(\mathbf{Q}_i\mathbf{x}\right)^T \neq 0$ or $\sum\limits_{j\in\mathcal{I}}\Gamma_{yj}\left(\mathbf{P}_j\mathbf{x}\right)\left(\mathbf{P}_j\mathbf{x}\right)^T \neq 0$. Furthermore, when $\mathbf{x}$ is given, there exists a positive constant L_1 such that

$$\| \bigtriangledown_{\mathbf{y}} \mathcal{G}(\mathbf{y}_1) - \bigtriangledown_{\mathbf{y}}\mathcal{G}(\mathbf{y}_2)\| \leq L_1\|\mathbf{y}_1-\mathbf{y}_2\|,\ \forall\, \mathbf{y}_1,\mathbf{y}_2\in\mathbb{R}^n. \tag{50}$$

which indicates that the gradient of $\mathcal{G}(\mathbf{x},\mathbf{y},\boldsymbol{\mu},\boldsymbol{\lambda})$ with respect to $\mathbf{y}$ is Lipschitz continuous, and the Lipschitz constant is simply the Frobenius norm of (49) for a fixed $\mathbf{x}$. For $\mathcal{F}(\mathbf{x},\mathbf{y},\boldsymbol{\nu},\boldsymbol{\lambda})$, the Hessian matrix with respect to $\mathbf{y}$ can be written as

$$\bigtriangledown^2_{\mathbf{y}}\mathcal{F} = \zeta_1\mathbf{I} + \zeta_3\sum_{j\in\mathcal{I}}\Gamma_{yj}\left(\mathbf{P}_j\mathbf{x}\right)\left(\mathbf{P}_j\mathbf{x}\right)^T. \tag{51}$$

Then, with $\zeta_1>0$ and $\zeta_3>0$, $\bigtriangledown^2_{\mathbf{y}}\mathcal{F}$ is positive definite. Given $\mathbf{x}$, there exists a constant $L_2>0$ such that

$$\| \bigtriangledown_{\mathbf{y}} \mathcal{F}(\mathbf{y}_1) - \bigtriangledown_{\mathbf{y}}\mathcal{F}(\mathbf{y}_2)\| \leq L_2\|\mathbf{y}_1-\mathbf{y}_2\|,\ \forall\, \mathbf{y}_1,\mathbf{y}_2\in\mathbb{R}^n. \tag{52}$$

Similarly, considering $\mathcal{H}(\mathbf{x},\mathbf{y},\boldsymbol{\nu},\boldsymbol{\mu})$, the Hessian matrix with respect to $\mathbf{y}$ is written as

$$\bigtriangledown^2_{\mathbf{y}}\mathcal{H} = \zeta_1\mathbf{I} + \zeta_2\sum_{i\in\mathcal{E}}\left(\mathbf{Q}_i\mathbf{x}\right)\left(\mathbf{Q}_i\mathbf{x}\right)^T. \tag{53}$$

Then, with $\zeta_1>0$ and $\zeta_2>0$, $\bigtriangledown^2_{\mathbf{y}}\mathcal{H}$ is also positive definite. When $\mathbf{x}$ is given, there exists a constant $L_3>0$ such that

$$\| \bigtriangledown_{\mathbf{y}} \mathcal{H}(\mathbf{y}_1) - \bigtriangledown_{\mathbf{y}}\mathcal{H}(\mathbf{y}_2)\| \leq L_3\|\mathbf{y}_1-\mathbf{y}_2\|,\ \forall\, \mathbf{y}_1,\mathbf{y}_2\in\mathbb{R}^n. \tag{54}$$

Therefore, $\mathcal{G}(\mathbf{x},\mathbf{y},\boldsymbol{\mu},\boldsymbol{\lambda})$, $\mathcal{F}(\mathbf{x},\mathbf{y},\boldsymbol{\nu},\boldsymbol{\lambda})$, and $\mathcal{H}(\mathbf{x},\mathbf{y},\boldsymbol{\nu},\boldsymbol{\mu})$ have Lipschitz continuous gradients with respect to $\mathbf{y}$. □

Theorem II.6. *Let Assumptions II.1 and II.2 hold, and $\{\mathbf{p}^k\}$ be a sequence with non-decreasing positive elements such that*

$$\frac{\kappa_y^k}{2} - \frac{(\beta+1)\,L_1^k}{2\zeta_1^k} - \frac{(\beta+1)\,L_2^k}{2\zeta_2^k} - \frac{|\mathcal{I}|\,(\beta+1)\,L_3^k}{2\zeta_3^k} > 0,$$
$$\forall\, k = 1,2,..,K, \tag{55}$$

where κ_y^k is the constant of κ_y^k-strongly convex Lagrangian $\mathcal{L}$ at kth step, $L_i, i=1,2,3$ are the Lipschitz constants of $\mathcal{G},\mathcal{F},\mathcal{H}$ at kth step, respectively. Let $\Lambda^0=[\boldsymbol{\nu}^0,\boldsymbol{\mu}^0,\boldsymbol{\lambda}^0]\neq\mathbf{0}$, then the sequence $\{\mathbf{x}^k,\mathbf{y}^k,\Lambda^k\}$ generated from Algorithm 1 will converge to a limit point and $\lim\limits_{k\to\infty}\left(\mathbf{x}^k-\mathbf{y}^k\right)=0$.

Proof. For the $\mathbf{x}$-update at kth step in (34a) with a given pair $(\mathbf{y}^k,\Lambda^k)$, there exists the following inequalities,

$$\begin{aligned}
&\mathcal{L}_{\mathbf{p}^k}(\mathbf{x}^k,\mathbf{y}^k,\Lambda^k) - \mathcal{L}_{\mathbf{p}^k}(\mathbf{x}^{k+1},\mathbf{y}^k,\Lambda^k)\\
\geq&\bigtriangledown_{\mathbf{x}}\mathcal{L}(\mathbf{x}^{k+1},\mathbf{y}^k,\Lambda^k)^T\left(\mathbf{x}^k-\mathbf{x}^{k+1}\right) + \frac{\kappa_x^k}{2}\left\|\mathbf{x}^k-\mathbf{x}^{k+1}\right\|^2\\
=&\frac{\kappa_x^k}{2}\left\|\mathbf{x}^k-\mathbf{x}^{k+1}\right\|^2 \geq \frac{\zeta_1^k}{2}\left\|\mathbf{x}^k-\mathbf{x}^{k+1}\right\|^2,
\end{aligned} \tag{56}$$

where the inequality holds due to the strong convexity of $\mathcal{L}_{\mathbf{p}^k}(\mathbf{x},\mathbf{y}^k,\Lambda^k)$ with respect to $\mathbf{x}$, the equality holds due to the first order optimality condition of (34a) with respect to $\mathbf{x}^{k+1}$. Similarly, for the $\mathbf{y}$-update at kth step in (34b) with a given pair

$(\mathbf{x}^{k+1}, \Lambda^k)$, we have the following inequality:

$$\mathcal{L}_{\mathbf{p}^k}(\mathbf{x}^{k+1}, \mathbf{y}^k, \Lambda^k) - \mathcal{L}_{\mathbf{p}^k}(\mathbf{x}^{k+1}, \mathbf{y}^{k+1}, \Lambda^k) \geq \frac{\kappa_y^k}{2}\left\|\mathbf{y}^k - \mathbf{y}^{k+1}\right\|^2. \tag{57}$$

On the other hand, consider the following first order optimality condition for the $\mathbf{y}$-update at the kth step

$$\bigtriangledown_{\mathbf{y}}\mathcal{L}_{\mathbf{p}^k} = \bigtriangledown_{\mathbf{y}}\mathcal{G}(\mathbf{y}^{k+1}) - \boldsymbol{\nu}^k + \zeta_1^k\left(\mathbf{y}^{k+1} - \mathbf{x}^{k+1}\right) = \mathbf{0}. \tag{58}$$

Combining (58) with the dual variable $\boldsymbol{\nu}$ update step in (34c), we obtain

$$\bigtriangledown_{\mathbf{y}}\mathcal{G}(\mathbf{y}^{k+1}) = \boldsymbol{\nu}^{k+1}. \tag{59}$$

Thus,

$$\begin{aligned}\left\|\boldsymbol{\nu}^{k+1} - \boldsymbol{\nu}^k\right\| &= \left\|\bigtriangledown_{\mathbf{y}}\mathcal{G}(\mathbf{y}^{k+1}) - \bigtriangledown_{\mathbf{y}}\mathcal{G}(\mathbf{y}^k)\right\| \\ &\leq L_1^k\left\|\mathbf{y}^{k+1} - \mathbf{y}^k\right\|,\end{aligned} \tag{60}$$

where the inequality holds due to the Lipschitz continuity of $\bigtriangledown_{\mathbf{y}}\mathcal{G}$ with respect to $\mathbf{y}$. For any given k, $\boldsymbol{\mu}^k$ and $\mathbf{y}^{k+1}$ are always updated in the same iteration. Then, we can rewrite the first order optimality condition of $\mathcal{L}_{\mathbf{p}}$ at kth step as

$$\begin{aligned}\bigtriangledown_{\mathbf{y}}\mathcal{L}_{\mathbf{p}^k} &= \bigtriangledown_{\mathbf{y}}\mathcal{F}(\mathbf{y}^{k+1}) + \left(\boldsymbol{\mu}^k\right)^T\mathbf{Q}_{\mathcal{E}}\mathbf{x}^{k+1} \\ &\quad + \zeta_2^k\left(\left(\mathbf{x}^{k+1}\right)^T\mathbf{Q}_{\mathcal{E}}\mathbf{y}^{k+1} - \mathbf{c}\right)\mathbf{Q}_{\mathcal{E}}\mathbf{x}^{k+1} \\ &= \mathbf{0}.\end{aligned} \tag{61}$$

Substituting the dual variable $\boldsymbol{\mu}$-update in (34d) into (61), we have

$$\nabla_{\mathbf{y}}\mathcal{F}(\mathbf{y}^{k+1}) = -\left(\boldsymbol{\mu}^{k+1}\right)^T\mathbf{Q}_{\mathcal{E}}\mathbf{x}^{k+1}. \tag{62}$$

Thus,

$$\begin{aligned}&\left\|\nabla_{\mathbf{y}}\mathcal{F}(\mathbf{y}^{k+1}) - \nabla_{\mathbf{y}}\mathcal{F}(\mathbf{y}^k)\right\| \\ &= \left\|\left(\boldsymbol{\mu}^{k+1}\right)^T\mathbf{Q}_{\mathcal{E}}\mathbf{x}^{k+1} - \left(\boldsymbol{\mu}^k\right)^T\mathbf{Q}_{\mathcal{E}}\mathbf{x}^k\right\|.\end{aligned} \tag{63}$$

For given $\mathbf{x}^{k+1}$ and $\mathbf{x}^k$, there exists a nonzero vector $\bar{\mathbf{x}}^{k+1}$ which is the linear combination of $\mathbf{x}^{k+1}$ and $\mathbf{x}^k$ such that

$$\begin{aligned}&\left\|\left(\boldsymbol{\mu}^{k+1}\right)^T\mathbf{Q}_{\mathcal{E}}\mathbf{x}^{k+1} - \left(\boldsymbol{\mu}^k\right)^T\mathbf{Q}_{\mathcal{E}}\mathbf{x}^k\right\| \\ &\geq \left\|\left(\mathbf{Q}_{\mathcal{E}}\bar{\mathbf{x}}^{k+1}\right)^T\left(\boldsymbol{\mu}^{k+1} - \boldsymbol{\mu}^k\right)\right\|.\end{aligned} \tag{64}$$

Note that either $\bar{\mathbf{x}}^{k+1} = \mathbf{x}^{k+1}$ or $\bar{\mathbf{x}}^{k+1} = \mathbf{x}^{k}$ will make (64) valid. Then, when Assumption II.2 holds, we have,

$$\left\| \left(\mathbf{Q}_{\mathcal{E}} \bar{\mathbf{x}}^{k+1} \right)^T \left(\boldsymbol{\mu}^{k+1} - \boldsymbol{\mu}^{k} \right) \right\| \geq \sigma_{\min}(\mathbf{Q}_{\mathcal{E}} \bar{\mathbf{x}}^{k+1}) \left\| \boldsymbol{\mu}^{k+1} - \boldsymbol{\mu}^{k} \right\| \tag{65}$$

Then, combining (63)-(65) and the Lipschitz continuity of the gradient $\bigtriangledown_{\mathbf{y}} \mathcal{F}$ with respect to $\mathbf{y}$ in (52), there exist a constant $L_2^k > 0$ such that

$$\left\| \boldsymbol{\mu}^{k+1} - \boldsymbol{\mu}^{k} \right\| \leq L_2^k \left\| \mathbf{y}^{k+1} - \mathbf{y}^{k} \right\|, \tag{66}$$

Similarly, we consider the update of $\boldsymbol{\lambda}$ at kth step. The first order optimality condition for the $\mathbf{y}$-update at the kth step can be written as

$$\begin{aligned} \bigtriangledown_{\mathbf{y}} \mathcal{L}_{\mathbf{p}^k} &= \bigtriangledown_{\mathbf{y}} \mathcal{H}(\mathbf{y}^{k+1}) + \left(\boldsymbol{\Gamma}_{\boldsymbol{y}}^{k+1} \circ \boldsymbol{\lambda}^{k} \right)^T \mathbf{P}_{\mathcal{I}} \mathbf{x}^{k+1} \\ &\quad + \zeta_3^k \boldsymbol{\Gamma}_{\boldsymbol{y}}^{k+1} \circ \left(\left(\mathbf{x}^{k+1} \right)^T \mathbf{P}_{\mathcal{I}} \mathbf{y}^{k+1} - \mathbf{d} \right) \mathbf{P}_{\mathcal{I}} \mathbf{x}^{k+1} \\ &= \mathbf{0}. \end{aligned} \tag{67}$$

Substituting the dual variable update in (34e) into (67), we have

$$\mathcal{H}(\mathbf{y}^{k+1}) = - \left(\boldsymbol{\Gamma}_{\boldsymbol{y}}^{k+1} \circ \boldsymbol{\lambda}^{k} \right)^T \mathbf{P}_{\mathcal{I}} \mathbf{x}^{k+1}. \tag{68}$$

Similarly, there exists a $\tilde{\mathbf{x}}^{k+1} \in \mathbb{R}^n$ such that

$$\begin{aligned} &\left\| \mathcal{H}(\mathbf{y}^{k+1}) - \mathcal{H}(\mathbf{y}^{k}) \right\| \\ &= \left\| \left(\boldsymbol{\Gamma}_{\boldsymbol{y}}^{k+1} \circ \boldsymbol{\lambda}^{k+1} \right)^T \mathbf{P}_{\mathcal{I}} \mathbf{x}^{k+1} - \left(\boldsymbol{\Gamma}_{\boldsymbol{y}}^{k} \circ \boldsymbol{\lambda}^{k} \right)^T \mathbf{P}_{\mathcal{I}} \mathbf{x}^{k} \right\| \\ &\geq \left\| \left(\boldsymbol{\Gamma}_{\boldsymbol{y}}^{k+1} \circ \boldsymbol{\lambda}^{k+1} - \boldsymbol{\Gamma}_{\boldsymbol{y}}^{k} \circ \boldsymbol{\lambda}^{k} \right)^T \mathbf{P}_{\mathcal{I}} \tilde{\mathbf{x}} \right\|. \end{aligned} \tag{69}$$

Combining Assumption II.2 and Lipschitz continuous gradient in (54), we can obtain the bounded constraint on dual variable $\boldsymbol{\lambda}$, expressed as

$$\left\| \boldsymbol{\Gamma}_{x}^{k+1} \circ \boldsymbol{\lambda}^{k+1} - \boldsymbol{\Gamma}_{y}^{k+1} \circ \boldsymbol{\lambda}^{k} \right\| \leq L_3^k \left\| \mathbf{y}^{k+1} - \mathbf{y}^{k} \right\|. \tag{70}$$

Next, we rewrite the successive difference of the augmented Lagrangian in the form

$$\begin{aligned} &\mathcal{L}_{\mathbf{p}^{k+1}}(\mathbf{x}^{k+1}, \mathbf{y}^{k+1}, \Lambda^{k+1}) - \mathcal{L}_{\mathbf{p}^{k}}(\mathbf{x}^{k}, \mathbf{y}^{k}, \Lambda^{k}) \\ &= \mathcal{L}_{\mathbf{p}^{k+1}}(\mathbf{x}^{k+1}, \mathbf{y}^{k+1}, \Lambda^{k+1}) - \mathcal{L}_{\mathbf{p}^{k}}(\mathbf{x}^{k+1}, \mathbf{y}^{k+1}, \Lambda^{k}) \\ &+ \mathcal{L}_{\mathbf{p}^{k}}(\mathbf{x}^{k+1}, \mathbf{y}^{k+1}, \Lambda^{k}) - \mathcal{L}_{\mathbf{p}^{k}}(\mathbf{x}^{k+1}, \mathbf{y}^{k}, \Lambda^{k}) \\ &+ \mathcal{L}_{\mathbf{p}^{k}}(\mathbf{x}^{k+1}, \mathbf{y}^{k}, \Lambda^{k}) - \mathcal{L}_{\mathbf{p}^{k}}(\mathbf{x}^{k}, \mathbf{y}^{k}, \Lambda^{k}). \end{aligned} \tag{71}$$

In the above equation, the subtraction

$$\mathcal{L}_{\mathbf{p}^{k+1}}(\mathbf{x}^{k+1},\mathbf{y}^{k+1},\Lambda^{k+1})-\mathcal{L}_{\mathbf{p}^{k}}(\mathbf{x}^{k+1},\mathbf{y}^{k+1},\Lambda^{k})$$

is bounded by

$$\begin{aligned}
&\mathcal{L}_{\mathbf{p}^{k+1}}(\mathbf{x}^{k+1},\mathbf{y}^{k+1},\Lambda^{k+1})-\mathcal{L}_{\mathbf{p}^{k}}(\mathbf{x}^{k+1},\mathbf{y}^{k+1},\Lambda^{k})\\
=&\left(\boldsymbol{\nu}^{k+1}-\boldsymbol{\nu}^{k}\right)^{T}\left(\mathbf{x}^{k+1}-\mathbf{y}^{k+1}\right)+\frac{\zeta_1^{k+1}-\zeta_1^{k}}{2}\left\|\mathbf{x}^{k+1}-\mathbf{y}^{k+1}\right\|^2\\
&+\left(\boldsymbol{\mu}^{k+1}-\boldsymbol{\mu}^{k}\right)^{T}\left(\left(\mathbf{x}^{k+1}\right)^{T}\mathbf{Q}_{\mathcal{E}}\mathbf{y}^{k+1}-\mathbf{c}\right)\\
&+\frac{\zeta_2^{k+1}-\zeta_2^{k}}{2}\left\|\left(\mathbf{x}^{k+1}\right)^{T}\mathbf{Q}_{\mathcal{E}}\mathbf{y}^{k+1}-\mathbf{c}\right\|^2\\
&+\left(\boldsymbol{\Gamma}_x^{k+1}\circ\boldsymbol{\lambda}^{k+1}-\boldsymbol{\Gamma}_y^{k}\circ\boldsymbol{\lambda}^{k}\right)^{T}\left(\left(\mathbf{x}^{k+1}\right)^{T}\mathbf{P}_{\mathcal{I}}\mathbf{y}^{k+1}-\mathbf{d}\right)\\
&+\frac{\zeta_3^{k+1}\|\boldsymbol{\Gamma}_x^{k+1}\|-\zeta_3^{k}\|\boldsymbol{\Gamma}_y^{k}\|}{2}\left\|\left(\mathbf{x}^{k+1}\right)^{T}\mathbf{P}_{\mathcal{I}}\mathbf{y}^{k+1}-\mathbf{d}\right\|^2\\
=&\frac{\zeta_1^{k+1}+\zeta_1^{k}}{2(\zeta_1^{k})^2}\left\|\boldsymbol{\nu}^{k+1}-\boldsymbol{\nu}^{k}\right\|^2+\frac{\zeta_2^{k+1}+\zeta_2^{k}}{2(\zeta_2^{k})^2}\left\|\boldsymbol{\mu}^{k+1}-\boldsymbol{\mu}^{k}\right\|^2\\
&+\frac{\zeta_3^{k+1}\|\boldsymbol{\Gamma}_x^{k+1}\|-\zeta_3^{k}\|\boldsymbol{\Gamma}_y^{k}\|}{2(\zeta_3^{k})^2}\left\|\boldsymbol{\Gamma}_x^{k+1}\circ\boldsymbol{\lambda}^{k+1}-\boldsymbol{\Gamma}_y^{k}\circ\boldsymbol{\lambda}^{k}\right\|^2\\
\leq&\frac{\beta+1}{2\zeta_1^{k}}\left\|\boldsymbol{\nu}^{k+1}-\boldsymbol{\nu}^{k}\right\|^2+\frac{\beta+1}{2\zeta_2^{k}}\left\|\boldsymbol{\mu}^{k+1}-\boldsymbol{\mu}^{k}\right\|^2\\
&+\frac{(\beta\|\boldsymbol{\Gamma}_x^{k+1}\|+\|\boldsymbol{\Gamma}_y^{k}\|)}{2\zeta_3^{k}}\left\|\boldsymbol{\Gamma}_x^{k+1}\circ\boldsymbol{\lambda}^{k+1}-\boldsymbol{\Gamma}_y^{k}\circ\boldsymbol{\lambda}^{k}\right\|^2
\end{aligned}\tag{72}$$

where the equality follows the definition of $\mathcal{L}$ and the update laws of Λ; the inequality holds due to the updating rules of penalty parameters in (35). Recall that $\mathcal{L}_{\mathbf{p}^{k}}(\mathbf{x}^{k+1},\mathbf{y}^{k+1},\Lambda^{k})-\mathcal{L}_{\mathbf{p}^{k}}(\mathbf{x}^{k+1},\mathbf{y}^{k},\Lambda^{k})$ and $\mathcal{L}_{\mathbf{p}^{k}}(\mathbf{x}^{k+1},\mathbf{y}^{k},\Lambda^{k})-\mathcal{L}_{\mathbf{p}^{k}}(\mathbf{x}^{k},\mathbf{y}^{k},\Lambda^{k})$ in (71) are bounded in (56) and (57) due to the strong convexity of $\mathcal{L}$ with respect to $\mathbf{x}$ and $\mathbf{y}$. Then, combining these inequalities, we have

$$\begin{aligned}
&\mathcal{L}_{\mathbf{p}^{k+1}}(\mathbf{x}^{k+1},\mathbf{y}^{k+1},\Lambda^{k+1})-\mathcal{L}_{\mathbf{p}^{k}}(\mathbf{x}^{k},\mathbf{y}^{k},\Lambda^{k})\\
=&\mathcal{L}_{\mathbf{p}^{k+1}}(\mathbf{x}^{k+1},\mathbf{y}^{k+1},\Lambda^{k+1})-\mathcal{L}_{\mathbf{p}^{k}}(\mathbf{x}^{k+1},\mathbf{y}^{k+1},\Lambda^{k})\\
&+\mathcal{L}_{\mathbf{p}^{k}}(\mathbf{x}^{k+1},\mathbf{y}^{k+1},\Lambda^{k})-\mathcal{L}_{\mathbf{p}^{k}}(\mathbf{x}^{k+1},\mathbf{y}^{k},\Lambda^{k})\\
&+\mathcal{L}_{\mathbf{p}^{k}}(\mathbf{x}^{k+1},\mathbf{y}^{k},\Lambda^{k})-\mathcal{L}_{\mathbf{p}^{k}}(\mathbf{x}^{k},\mathbf{y}^{k},\Lambda^{k})\\
\leq&-\frac{\kappa_x^{k}}{2}\left\|\mathbf{x}^{k+1}-\mathbf{x}^{k}\right\|^2-\frac{\kappa_y^{k}}{2}\left\|\mathbf{y}^{k+1}-\mathbf{y}^{k}\right\|^2\\
&+\frac{\beta+1}{2\zeta_1^{k}}\left\|\boldsymbol{\nu}^{k+1}-\boldsymbol{\nu}^{k}\right\|^2+\frac{\beta+1}{2\zeta_2^{k}}\left\|\boldsymbol{\mu}^{k+1}-\boldsymbol{\mu}^{k}\right\|^2\\
&+\frac{(\beta\|\boldsymbol{\Gamma}_x^{k+1}\|+\|\boldsymbol{\Gamma}_y^{k}\|)}{2\zeta_3^{k}}\left\|\boldsymbol{\Gamma}_x^{k+1}\circ\boldsymbol{\lambda}^{k+1}-\boldsymbol{\Gamma}_y^{k}\boldsymbol{\lambda}^{k}\right\|^2\\
\leq&-\frac{\kappa_x^{k}}{2}\left\|\mathbf{x}^{k+1}-\mathbf{x}^{k}\right\|^2\\
&-\left(\frac{\kappa_y^{k}}{2}-\frac{(\beta+1)L_1^{k}}{2\zeta_1^{k}}-\frac{(\beta+1)L_2^{k}}{2\zeta_2^{k}}\right)\left\|\mathbf{y}^{k+1}-\mathbf{y}^{k}\right\|^2
\end{aligned}$$

$$- \left(\frac{(\beta \|\mathbf{\Gamma}_x^{k+1}\| + \|\mathbf{\Gamma}_y^k\|) L_3^k}{2\zeta_3^k} \right) \left\|\mathbf{y}^{k+1} - \mathbf{y}^k\right\|^2, \tag{73}$$

where the last inequality is due to (60), (66) and (70). In addition, based on the definitions of Γ_x and Γ_y in (37) and (41), we have $\|\Gamma_x\| \leq |\mathcal{I}|$ and $\|\Gamma_y\| \leq |\mathcal{I}|$. Therefore,

$$\begin{aligned}
&\mathcal{L}_{\mathbf{p}^{k+1}}(\mathbf{x}^{k+1}, \mathbf{y}^{k+1}, \Lambda^{k+1}) - \mathcal{L}_{\mathbf{p}^k}(\mathbf{x}^k, \mathbf{y}^k, \Lambda^k) \\
\leq & -\frac{\kappa_x^k}{2}\left\|\mathbf{x}^{k+1} - \mathbf{x}^k\right\|^2 \\
& - \left(\frac{\kappa_y^k}{2} - \frac{(\beta+1)L_1^k}{2\zeta_1^k} - \frac{(\beta+1)L_2^k}{2\zeta_2^k} \right) \left\|\mathbf{y}^{k+1} - \mathbf{y}^k\right\|^2 \\
& - \left(\frac{|\mathcal{I}|(\beta+1)L_3^k}{2\zeta_3^k} \right) \left\|\mathbf{y}^{k+1} - \mathbf{y}^k\right\|^2.
\end{aligned} \tag{74}$$

The above result implies that when satisfying the condition in (55), the value of the augmented Lagrangian function is non-increasing. Note that as long as $\kappa_y^k \neq 0$, one can always find a $\mathbf{p}^k$ with sufficiently large elements $[\zeta_1^k, \zeta_2^k, \zeta_3^k]$ to satisfy the above condition. Furthermore, by summing both sides in (74) from $k = 0$ to ∞, we obtain

$$\begin{aligned}
&\mathcal{L}_{\mathbf{p}^\infty}(\mathbf{x}^\infty, \mathbf{y}^\infty, \Lambda^\infty) - \mathcal{L}_{\mathbf{p}^0}(\mathbf{x}^0, \mathbf{y}^0, \Lambda^0) \\
& \leq -\sum_{k=0}^{\infty} \frac{\kappa_x^k}{2}\left\|\mathbf{x}^{k+1} - \mathbf{x}^k\right\|^2 - \sum_{k=0}^{\infty} \frac{\hat{\kappa}_y^k}{2}\left\|\mathbf{y}^{k+1} - \mathbf{y}^k\right\|^2.
\end{aligned} \tag{75}$$

where $\hat{\kappa}_y = \kappa_y^k - \frac{(\beta+1)L_1^k}{\zeta_1^k} - \frac{(\beta+1)L_2^k}{\zeta_2^k} - \frac{|\mathcal{I}|(\beta+1)L_3^k}{\zeta_3^k}$. With Assumption II.1 holding, the Augmented Lagrange function is lower bounded. Then, in (75), both $\sum_{k=0}^{\infty} \frac{\kappa_x^k}{2}\|\mathbf{x}^{k+1} - \mathbf{x}^k\|^2$ and $\sum_{k=0}^{\infty} \frac{\hat{\kappa}_y^k}{2}\|\mathbf{y}^{k+1} - \mathbf{y}^k\|^2$ are upper bounded. In other words, the sequences $\{\mathbf{x}^k\}$ and $\{\mathbf{y}^k\}$ will converge to limit points. Moreover, due to the constraint $\|\boldsymbol{\nu}^{k+1} - \boldsymbol{\nu}^k\| \leq L_1^k\|\mathbf{y}^{k+1} - \mathbf{y}^k\|$ in (60), the sequence $\{\boldsymbol{\nu}^k\}$ will also converge to a limit point, denoted as $\boldsymbol{\nu}^\infty$. Meanwhile, by taking the limits on both sides of (34c), we have

$$\lim_{k\to\infty} \boldsymbol{\nu}^{k+1} = \lim_{k\to\infty} \left(\boldsymbol{\nu}^k + \zeta_1^k \left(\mathbf{x}^{k+1} - \mathbf{y}^{k+1} \right) \right), \tag{76}$$

which leads to $\lim_{k\to\infty} (\mathbf{x}^{k+1} - \mathbf{y}^{k+1}) = 0$. □

Theorem II.7. *Let* $\{\mathbf{x}^k\}$ *and* $\{\mathbf{y}^k\}$ *be the sequences obtained from Algorithm 1, if* $\lim_{k\to\infty} \left(\mathbf{x}^{k+1} - \mathbf{x}^k\right) = 0$ *and* $\lim_{k\to\infty} \left(\mathbf{x}^k - \mathbf{y}^k\right) = 0$*, then the limit point of* $\{\mathbf{x}^k\}$ *is a stationary point of problem* (30)*.*

Proof. A Karush–Kuhn–Tucker (KKT) point $\mathbf{x}^*$ of problem (30) with the corresponding dual variables μ^* and λ^* satisfies that

$$\mathbf{Q}_0\mathbf{x}^* + \sum_{i\in\mathcal{E}} \mu_i^*\mathbf{Q}_i\mathbf{x}^* + \sum_{j\in\mathcal{I}} \lambda_j^*\mathbf{P}_j\mathbf{x}^* = 0 \tag{77a}$$

$$\mu_i^* \left((\mathbf{x}^*)^T \mathbf{Q}_i\mathbf{x}^* + c_i \right) = 0, \ \forall i \in \mathcal{E} \tag{77b}$$

$$\lambda_j^* \left((\mathbf{x}^*)^T \mathbf{P}_j\mathbf{x}^* + d_j \right) = 0, \ \forall j \in \mathcal{I} \tag{77c}$$

$$\left((\mathbf{x}^*)^T \mathbf{Q}_i\mathbf{x}^* + c_i \right) = 0 \tag{77d}$$

$$\left((\mathbf{x}^*)^T \mathbf{P}_j \mathbf{x}^* + d_j\right) \leq 0 \tag{77e}$$

$$\lambda_j \geq 0 \tag{77f}$$

With $\lim_{k\to\infty}(\mathbf{x}^{k+1} - \mathbf{x}^k) = 0$ and $\lim_{k\to\infty}(\mathbf{x}^k - \mathbf{y}^k) = 0$, $\{\mathbf{x}^k\}$ and $\{\mathbf{y}^k\}$ will converge to a limit point, denoted as $\mathbf{x}^\infty = \mathbf{y}^\infty$. Moreover, considering the bounded dual variables in (60) and (70), $\{\Lambda^k\}$ will converge to a limit point denoted as Λ^∞. Then Λ^∞ also satisfies the first order optimality conditions of subproblems (34a) and (34b), expressed as

$$\begin{aligned}&\mathbf{Q}_0\mathbf{y}^\infty + \nu^\infty\mathbf{I} + \sum_{i\in\mathcal{E}}(\mu_i^\infty \mathbf{Q}_i\mathbf{y}^\infty)\\ &+\sum_{j\in\mathcal{I}}\Gamma_{xj}^\infty\left(\lambda_j^\infty\mathbf{P}_j\mathbf{y}^\infty\right) = 0\end{aligned} \tag{78a}$$

$$\begin{aligned}&\mathbf{Q}_0\mathbf{x}^\infty - \nu^\infty\mathbf{I} + \sum_{i\in\mathcal{E}}(\mu_i^\infty \mathbf{Q}_i\mathbf{x}^\infty)\\ &+\sum_{j\in\mathcal{I}}\Gamma_{yj}^\infty\left(\lambda_j^\infty\mathbf{P}_j\mathbf{x}^\infty\right) = 0\end{aligned} \tag{78b}$$

$$\mu_i^\infty\left((\mathbf{x}^\infty)^T\mathbf{Q}_i\mathbf{y}^\infty + c_i\right) = 0, \forall i \in \mathcal{E} \tag{78c}$$

$$\lambda_j^\infty\left((\mathbf{x}^\infty)^T\mathbf{P}_j\mathbf{y}^\infty + d_j\right) = 0, \forall j \in \mathcal{I} \tag{78d}$$

$$\left((\mathbf{x}^\infty)^T\mathbf{Q}_i\mathbf{y}^\infty + c_i\right) = 0 \tag{78e}$$

$$\left((\mathbf{x}^\infty)^T\mathbf{P}_j\mathbf{y}^\infty + d_j\right) \leq 0 \tag{78f}$$

$$\lambda_j^\infty \geq 0 \tag{78g}$$

When the limit points satisfy $\mathbf{x}^\infty = \mathbf{y}^\infty$, $\Gamma_{xj}^\infty = \Gamma_{yj}^\infty$, the summation of (78a) and (78b) and (78c)-(78g) lead to the same KKT conditions in (77). Thus, the limit point of $\{\mathbf{x}^k\}$ is a stationary point of problem (30). □

III. Simulation Results

In this section, we present simulation results obtained using the proposed ADMM algorithm and comparative results obtained from a commercial NLP solver [44]. All simulations were run in MatLab on a 3.6 GHz Desktop with 32 GB RAM. In §III-A and III-B, the proposed ADMM is first applied to solve the guidance problems for Mars entry phase and powered descent phase separately. Next, the proposed algorithm is applied to solve the fuel-optimal end-to-end EDL guidance problem in §III-C. Comparative results obtained from the NLP solver for the same problems are presented to demonstrate the effectiveness of the proposed ADMM algorithm. Monte-Carlo simulations are provided in §III.D to demonstrate the robustness of the proposed algorithm. For all simulation cases, the convergence criterion is set as $\epsilon = 1e-4$, and the sequences of three weighting factors $\{\zeta_1^k\}, \{\zeta_2^k\}, \{\zeta_3^k\}$ are generated via (35) with $\zeta_1^0 = 1e2$, $\beta_1 = 1.4$, $\zeta_2^0 = 5e3$, $\beta_2 = 1.5$, $\zeta_3^0 = 3$, $\beta_3 = 1.2$, $\tau = 1$, $\zeta_{1_{\max}} = 5e5$, $\zeta_{2_{\max}} = 5e6$, $\zeta_{3_{\max}} = 5e2$.

A. Results for Optimal Guidance of Entry Phase

We are using the Hypersonic Inflatable Aerodynamic Decelerator (HIAD) in [10] as the landing vehicle, shown in Fig. 4. Specifically, the shape of the landing vehicle can be represented by a symmetric sphere cone with 20 m diameter. The entry

mass m_0 is assumed to be 51.099 tons. The lift and drag coefficients of the vehicle C_L and C_D are obtained from [45], where $c_{d0} = 1.572, c_{d1} = -0.0092$, and $c_{d2} = -2.242$. The upper and lower bounds on C_L are set as $0 \leq C_L \leq 0.38$. The initial states of the entry vehicle are given by $R_0 = R_m + 100$ km and $V_0 = 4700\,\text{m/s}$. The initial flight path angle is given as $\gamma_0 = -10.8^\circ$. The bounds on the terminal radius of the entry phase are $R_I^L = R_m + 7\,\text{km}$ and $R_I^U = R_m + 12\,\text{km}$. The other parameters for the entry phase guidance problem are set as

$$
\begin{aligned}
&k_Q = 1.9027 \times 10^{-8} \times (\sqrt{h_0 g_0})^{3.15},\ Q_{\max} = 800\,\text{W/cm}^2,\\
&\bar{q}_{\max} = 14000\,\text{N/m}^2, n_{\max} = 2.5 g_E,\ g_E = 9.8\,\text{m/s}^2,\\
&g_0 = 3.7114\,\text{m/s}^2,\ S = \frac{20^2 \cdot \pi}{4}\,\text{m}^2.
\end{aligned}
$$

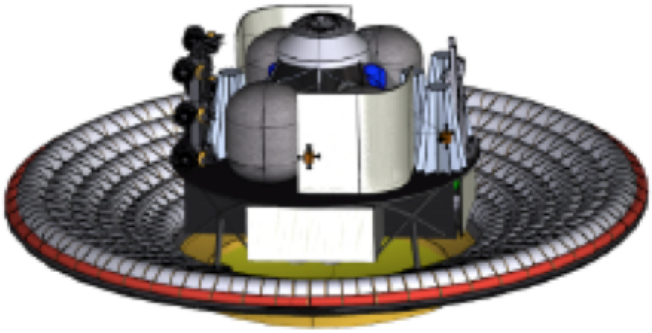

Fig. 4: Hypersonic Inflatable Aerodynamic Decelerator in [10]

By discretizing the entry phase trajectory into 50 intervals, it takes 99 iterations and 16.1 seconds for the customized ADMM to obtain a converged result. The initial guess used for the customized ADMM is generated by giving a linear control C_L varying from $C_{L\min}$ to $C_{L\max}$, and then integrating the dynamics forward till the radius reaches the specified lower bound. The simulation results are shown in Figs. 5-7. Specifically, Fig. 5 demonstrates time histories of C_L and C_D obtained from the customized ADMM and an NLP solver. The duration results from both methods, 278.4 seconds for ADMM and 274.7 seconds for NLP, are close to each other. The time histories of the states variables from both methods are similar, as shown in Fig. 6, where the red-circled curves represent the ADMM solution and the blue star curves represent the NLP solution. For the time histories of states, the integrated curves and the solution of ADMM are almost overlapping with each other. The blue solid line in Fig. 6b represents the heating rate boundary during the entry phase. Furthermore, Fig. 7 shows the time histories of dynamic pressure and normal load, where the blue solid lines are the upper bounds of the dynamic pressure and normal load constraints. The terminal velocity of the entry phase obtained from ADMM is 327.2 m/s at an altitude of 7001.4 m, which is very close to the terminal speed obtained from the NLP solver, that is 328.8 m/s at an altitude of 7018.5 m.

B. Results for Optimal Guidance of the Powered Descent Phase

For the powered descent phase, we assume that the initial position and velocity are the final states of entry trajectories obtained from §IV.III-A. For fair comparison, we use the final states of entry trajectories obtained from ADMM and NLP,

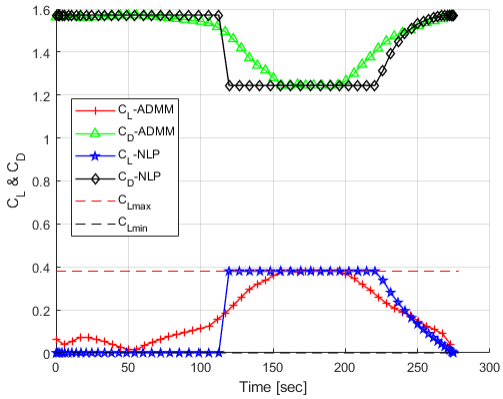

Fig. 5: Time histories of C_L and C_D from ADMM and NLP solver

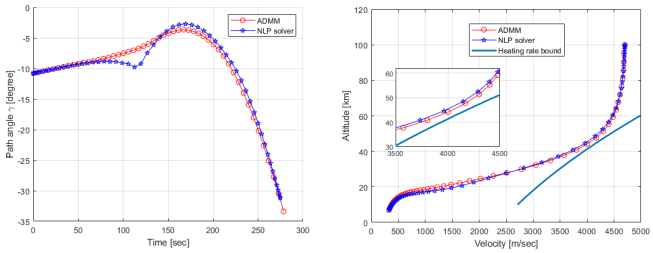

(a) Time histories of of flight path angle (b) Reference altitude vs. velocity

Fig. 6: Time histories of state variables during the entry phase from both methods

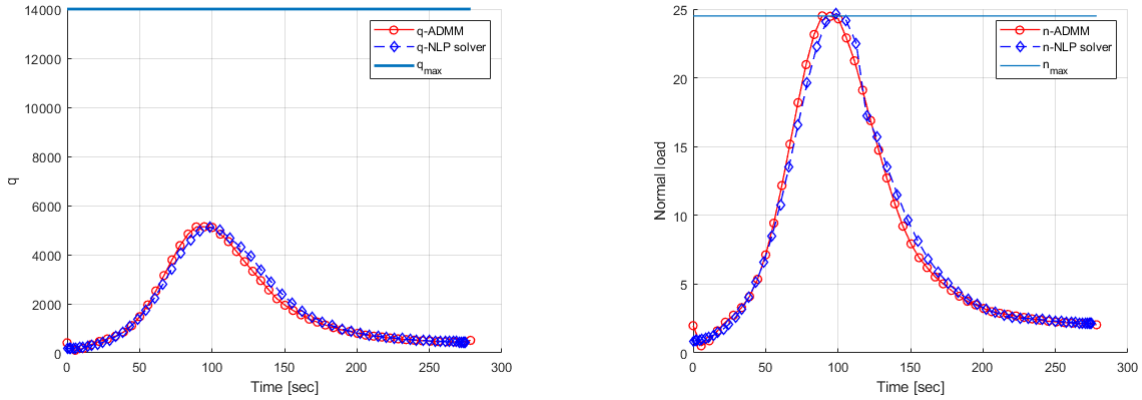

(a) Time history of dynamic pressure (b) Time history of normal load

Fig. 7: Time histories of mission constraints during the entry phase

respectively, as the corresponding initial conditions of the powered descent phase when using both methods again for guidance in this phase. Specifically, the terminal states of the entry phase obtained from the ADMM are $z(t_I) = 7001.4\,\text{m}$, $v_x(t_I) = V\cos(\gamma) = 273.3\,\text{m/s}$, $v_z(t_I) = V\sin(\gamma) = -180.0\,\text{m/s}$, and the corresponding ones obtained from NLP are $z(t_I) = 7018.5\,\text{m}$, $v_x(t_I) = V\cos(\gamma) = 281.1\,\text{m/s}$, $v_z(t_I) = V\sin(\gamma) = -170.4\,\text{m/s}$. In addition, we assume $x(t_I) = 0$, and the parameters in the equations of motion for the powered descent phase are set as

$$\mathbf{g} = [0, -3.7114]^T\,\text{m/s}^2,\ m_{\text{pdi}} = 51099\,\text{kg},$$

$$
\begin{aligned}
&m_{\text{dry}} = 0.8 m_{\text{pdi}} = 40880\,\text{kg},\ \eta = 4.53 \times 10^{-5}\text{s/m},\\
&T_{\max} = 800\text{kN} * 0.8 = 640\,\text{kN},\\
&T_{\min} = 0.3 * 800\,\text{kN} = 240\,\text{kN}.
\end{aligned} \tag{79}
$$

The maximum glide-slope angle is set as $\theta = 86^\circ$. The trajectory for the powered-descent phase is discretized into 92 intervals. Figures 8 and 9 present the results generated for the powered descent phase using the proposed ADMM and an NLP solver, respectively. Note that the powered descent trajectory of the NLP solver is discretized by 60 nodes, which is the maximum number of nodes for the NLP to achieve a converged solution. The simulation took 3.1 seconds and 51 iterations for ADMM to obtain a converged result that consumes 1561.8 kg of fuel and 72.3 seconds to land on the designated landing site. In contrast, the calculation time of the NLP solver is 8.1 seconds and the solution from NLP consumes 1498.5 kg fuel and 73.1 seconds for landing.

Comparing the thrust profiles in Fig. 8a, the solutions from ADMM and NLP are close to a bang-bang control profile with max-min-max arcs. Obviously, the entry phase and the powered descent phase are coupled in the transition conditions including the altitude and the velocity components at the transition point. Therefore, the optimal guidance laws of both phases, as well as the transition point, need to be determined together when searching for the fuel-optimal end-to-end EDL trajectory.

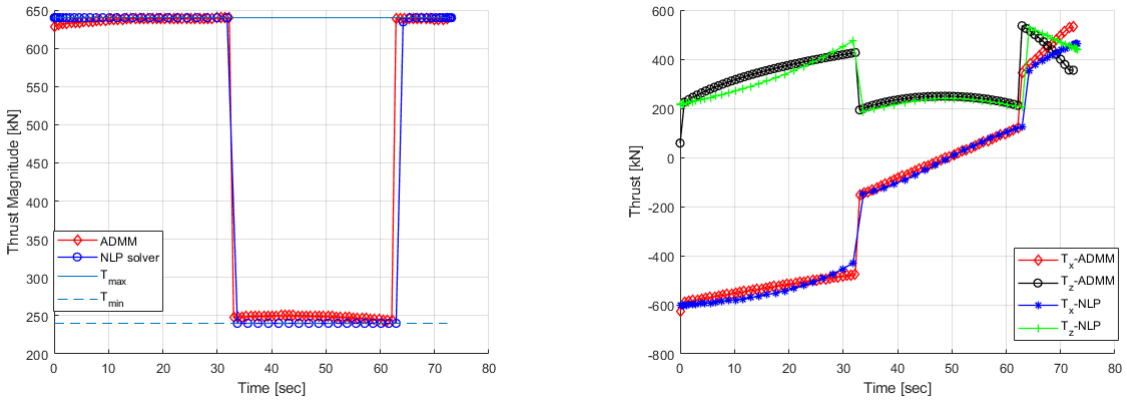

(a) Time history of control magnitude $\|\mathbf{T}\|$ (b) Time history of control components T_x and T_z

Fig. 8: Time histories of control magnitude and components for the powered descent phase from ADMM and NLP

C. Results for Optimal Guidance of the End-to-End EDL Mission

In the end-to-end EDL problem, all settings in the simulation, including the spacecraft parameters, the initial states of the entry phase, the terminal conditions of the powered descent phase, and the constraints in both phases are the same as those in §IV.III-A and §IV.III-B. But the ignition position and time are unknown and to be determined. Moreover, we consider an inequality constraint on the x coordinate of the transition point, i.e. $x(t_I) \in [-10, 10]$ km. Then both ADMM and NLP are applied to solve the end-to-end EDL guidance problem with the same initial and terminal conditions. Since the NLP solver requires a good combination of the number of discrete nodes and initial guess to find a converged solution, both the entry phase trajectory and the powered descent phase trajectory are discretized into 60 nodes. In order to improve the accuracy of ADMM

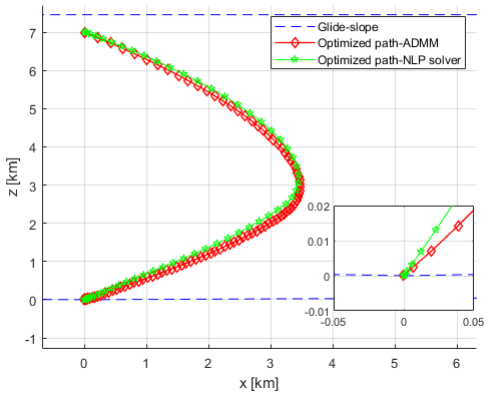

(a) Optimized trajectory

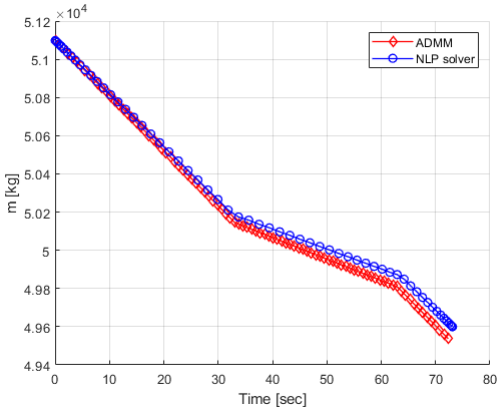

(b) Time history of mass

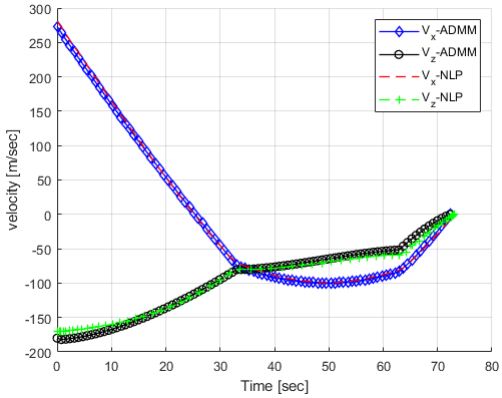

(c) Time history of velocity components v_z

Fig. 9: Trajectory and time histories of state variables for the powered descent phase from the ADMM and the NLP solver

solution, the trajectory in the powered descent phase for ADMM is discretized into 93 nodes. As a result, the homogeneous QCQP problem of (29) includes 1869 unknown variables. Moreover, the initial guess for NLP is obtained from the solution of separated phase path planning in §IV.III-A and §IV.III-B. It takes the customized ADMM 73.2 seconds and 210 iterations to find a converged solution. However, the NLP solver fails to find a converged solution under this scenario when setting a free $x(t_I)$ for the powered descent phase, which in turn shows the effectiveness of the proposed ADMM in solving the large-scale end-to-end EDL guidance problem.

In order to obtain comparative results from the NLP solver, we let $x(t_I) = 0$ for the powered descent phase in the end-to-end EDL mission. Under this setting, the problem is solved by ADMM and NLP, separately. The comparison of mission duration, fuel consumption, and computation time from the separate phase guidance and the end-to-end EDL guidance using ADMM and NLP are summarized in Table I. The time histories of the control and state variables of the end-to-end EDL mission are shown in Figs. 10 and 11, respectively. Figures 10a shows the optimized control profiles, C_L and C_D, from ADMM with a free $x(t_I)$, ADMM with a fixed $x(t_I)$, and NLP in entry phase, respectively. When $x(t_I)$ is free, the optimized $x^*(t_I)$ is -5.52 km, and the velocity at the transition point from the ADMM solution is 298.3 m/s at the altitude of 7000.5 m. However, with a fixed $x(t_I) = 0$, the speed at the end of entry phase in the ADMM solution is 315.5 m/s at an altitude of 6912.8 m, while the speed from NLP is 329.4 m/s at 6995 m.

Figures 10b and 10c present the thrust components and magnitude in powered-descent phase from two methods. The trajectories and time histories of state variables obtained from ADMM and NLP are shown in Fig.11. When $x(t_I)$ is free, the terminal mass of the landing vehicle from the ADMM solution is about 50087.0 kg, which indicates that the landing vehicle only consumes 1012.0 kg of fuel during the powered descent phase. However, if $x(t_I)$ is fixed at 0, the landing vehicle consumes 1494.8 kg of fuel during the powered descent phase in the ADMM solution. In contrast, the NLP solution of the end-to-end mission consumes 1496.2 kg of fuel, which is 484.2 kg less than the fuel consumption in the ADMM solution with the fixed $x(t_I)$ and 1.4 kg more than that from the ADMM with a free $x(t_I)$. In addition, the time histories of the dynamic pressure and the normal load during the entry phase are presented in Fig. 13, which shows that for the ADMM solution, the normal load inequality constraint is active at about 100 seconds during the entry phase.

From Tables 1, several conclusions can be drawn: (1) Solutions from both ADMM and NLP show the advantages of end-to-end EDL planning strategy in terms of fuel-saving by comparing to the corresponding solutions obtained from separate phase planning, especially for the case with unfixed x coordinate at the transition point; (2) The comparison of the computational time of both methods shows the computational efficiency of the proposed ADMM algorithm in solving the end-to-end EDL guidance problem. The observation of improved fuel efficiency of the end-to-end EDL guidance is consistent with our expectation that optimizing the transition point between the two phases will further improve the fuel efficiency.

TABLE I: Comparison of mission duration, fuel consumption, and computation time for separate phase guidance and end-to-end EDL guidance using ADMM and NLP: Case 1: End-to-end guidance from ADMM with a fixed $x(t_I)$; Case 2: End-to-end guidance from ADMM with a free $x(t_I)$; Case 3: End-to-end guidance from NLP with a fixed $x(t_I)$; Case 4: Separate phase guidance from ADMM; Case 5: Separate phase guidance from NLP.

	t_I (sec)	t_f (sec)	Fuel (kg)	Computational time (sec)
Case 1	293.0	362.5	1494.8	50.7
Case 2	301.6	348.7	1012.0	51.2
Case 3	274.1	346.4	1496.2	78.1
Case 4	278.4	350.7	1561.8	16.1+3.1
Case 5	274.7	347.8	1498.5	1.5+8.1

D. Robust Analysis of the End-to-End EDL Mission Guidance

In this section, we aim to verify the robustness and computational efficiency of the proposed algorithm in generating optimal end-to-end trajectories given initial conditions within a specified range. Specifically, we consider changes of the initial conditions around the nominal initial altitude $R_0 = R_m + 100$ km and velocity $V_0 = 4700$ m/s, where the nominal values are selected from the problem settings in §IV.III-C. Accordingly, the initial altitude and velocity are set as

$$R(t_0) = R_0 + \delta r,\ V(t_0) = V_0 + \delta V, \tag{80}$$

where δr is assumed to have a zero-mean normal distribution with an independent standard deviation of 5 km, and δV is assumed to have a zero-mean normal distribution with an independent standard deviation of 50 m/s.

We generate 1000 cases with different initial altitudes and velocities using the above normal distributions, shown in Fig. 14a. All of these 1000 cases converge to local optimum points. Moreover, Fig. 14b shows the fuel consumption of these 1000 cases,

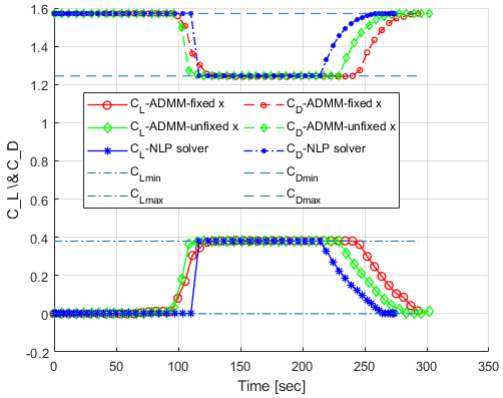

(a) Time histories of C_L in the entry phase

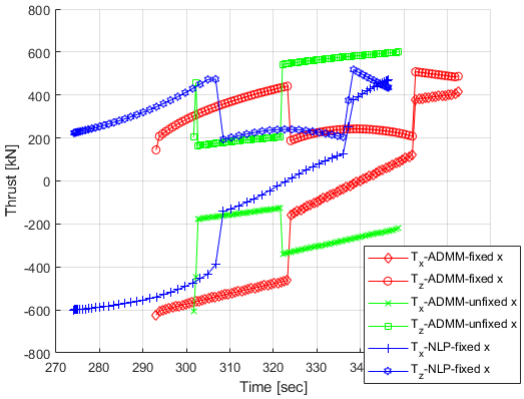

(b) Time histories of thrust components in the powered descent phase

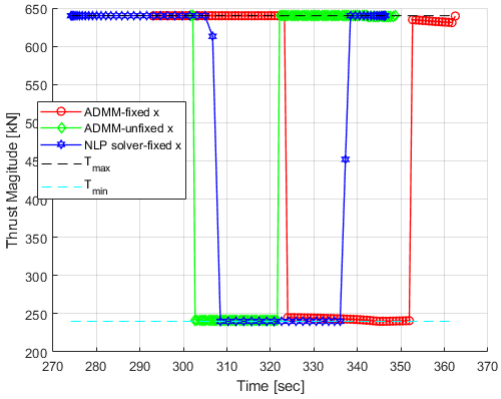

(c) Time histories of thrust magnitude in the powered descent phase

Fig. 10: Time histories of control variables for the end-to-end EDL mission from ADMM and NLP

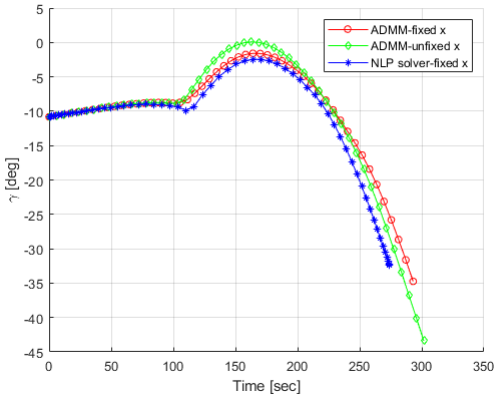

(a) Time history of flight path angle γ

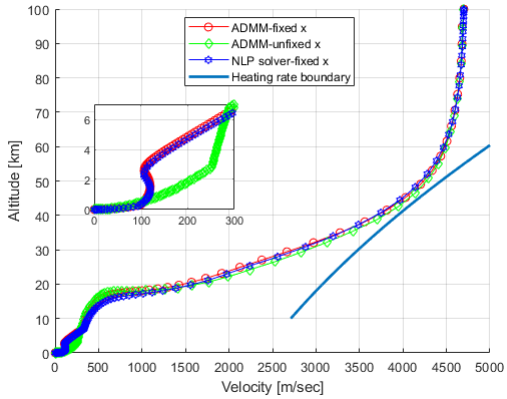

(b) Altitude vs. speed

Fig. 11: Trajectory and time histories of state variables for the end-to-end EDL mission from ADMM and NLP

where the mean fuel consumption value is 1091.8 kg and the standard deviation is 724.0 kg. Figure 14c shows the computational time of all 1000 cases, where 65% cases only takes less than 60 seconds to find a converged solution, and the computational time of the other cases vary from 70 seconds to 140 seconds. The average computational time of these 1000 cases is 64.4 seconds. These simulation results support the conclusion that the algorithm's results do not change appreciably for any initial

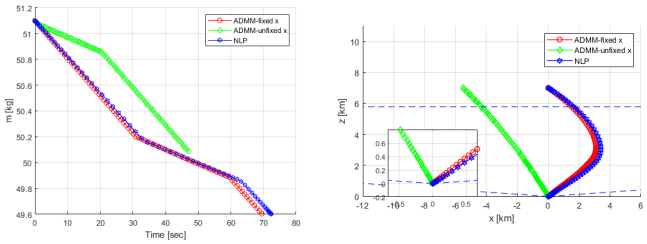

(a) Time history of mass in powered-descent phase

(b) Optimized trajectories in Powered descent phase

Fig. 12: Trajectory and time histories of state variables for the end-to-end EDL mission from ADMM and NLP

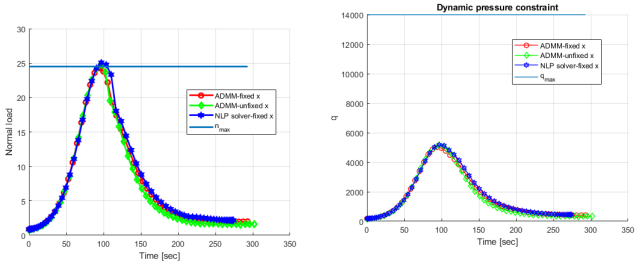

(a) Normal load in entry phase

(b) Dynamic pressure in entry phase

Fig. 13: Time histories of normal load and dynamic pressure for the end-to-end EDL mission from ADMM and NLP

conditions in the tested range.

In a summary, by integrating the separate guidance problems of the entry phase and powered descent phase into an end-to-end EDL guidance problem, we have more flexibility to plan the entire EDL mission, which leads to a solution with less fuel consumption. Meanwhile, since the fuel required for EDL mission only takes less than 40% of the entire fuel capacity, the vehicle could be designed with smaller fuel capacity, which will reduce the vehicle mass. Moreover, the simulation results under different problem settings, i.e., free and fixed $x(t_I)$, validate the effectiveness and robustness of the customized ADMM for solving the large-scale multi-phase EDL guidance problem compared to the NLP solver. Furthermore, each iteration of the ADMM is a closed-form update based on simple linear vector/matrix operations. In other words, the ADMM does not require any optimization solver, which makes it highly implementable for real-time computations.

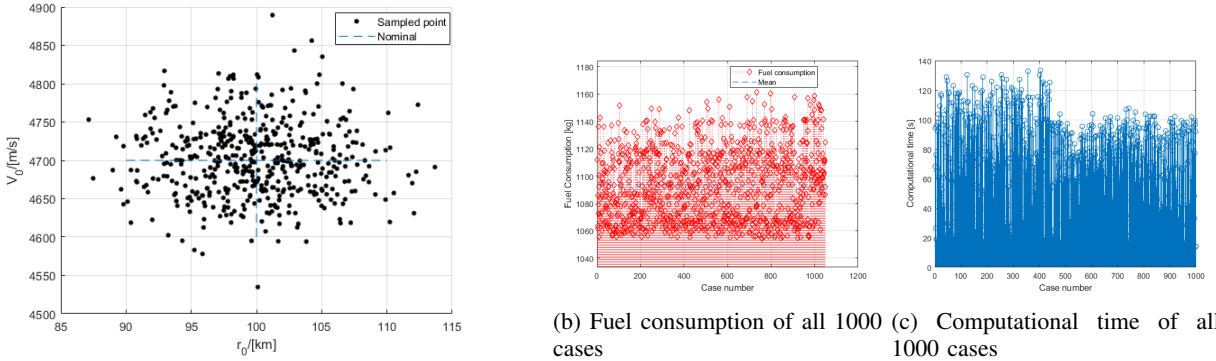

(a) Initial position and velocity dispersion with respect to the nominal values.

(b) Fuel consumption of all 1000 cases

(c) Computational time of all 1000 cases

Fig. 14: Fuel consumption and computational time of all 1000 cases.

IV. Conclusions

This paper has investigated the fuel-optimal guidance of the end-to-end human-Mars entry, powered descent and landing (EDL) mission by planning the entire decent sequence as a whole. We first modeled the end-to-end EDL problem as a multi-phase optimal control problem with different dynamics and constraints at each phase. Via polynomial approximation and discretization techniques, this multi-phase optimal control problem is reformulated as a polynomial programming problem which is then equivalently converted into a nonconvex quadratically constrained quadratic programming problem. A customized alternating direction method of multipliers is developed to solve large-scale nonconvex QCQPs based on simple linear matrix operations. Convergence analysis of the proposed algorithm is provided under certain conditions on algorithmic parameters. Finally, the comparative simulation results validate the improved fuel efficiency of the end-to-end EDL guidance compared with the fuel consumption amount obtained from both end-to-end planning and separate phase guidance. Moreover, the computational efficiency and robustness in terms of calculation time and convergence of the customized ADMM algorithm has been verified through comparison with the state-of-art nonlinear programming (NLP) method and analysis of uncertainty on initial altitude and velocity. When handling large-scale QCQP problems with more than one thousand unknown variables, the proposed algorithm can find a local optimum within several seconds in Matlab computational environments. The proposed formulation and algorithm can be applied to other challenging mission planning problems where the system is characterized with varying dynamics and/or constraints. Our future work will focus on extending the human-mars EDL problem to three dimensions, and further improving the computational efficiency.

References

[1] R. D. Braun and R. M. Manning, "Mars exploration entry, descent, and landing challenges," *Journal of Spacecraft and Rockets*, vol. 44, no. 2, pp. 310–323, 2007.

[2] P. I. Andre Makovsky and J. Taylor, "Mars science laboratory telecommunications system design," 2009.

[3] A. D. Cianciolo and T. T. Polsgrove, "Human mars entry, descent, and landing architecture study overview," 2016.

[4] R. D. Braun, B. Sforzo, and C. Campbell, "Advancing supersonic retropropulsion using mars-relevant flight data: An overview," in *AIAA SPACE and Astronautics Forum and Exposition*, 2017.

[5] T. Zang, A. Dwyer-Cianciolo, M. Ivanov, R. Sostaric, and D. Kinney, "Overview of the nasa entry, descent and landing systems analysis studies for large robotic-class missions," in *AIAA SPACE 2011 Conference & Exposition*, 2011.

[6] A. M. DwyerCianciolo, T. A. Zang, R. R. Sostaric, and M. K. McGuire, "Overview of the nasa entry, descent and landing systems analysis exploration feed-forward study," in *International Planetary Probe Workshop*, 2011.

[7] J. R. Rea, *An investigation of fuel optimal terminal descent*. PhD thesis, The University of Texas at Austin, 2009.

[8] J. A. Leavitt and K. D. Mease, "Feasible trajectory generation for atmospheric entry guidance," *Journal of Guidance, Control, and Dynamics*, vol. 30, no. 2, pp. 473–481, 2007.

[9] C. Zimmerman, G. Dukeman, and J. Hanson, "Automated method to compute orbital reentry trajectories with heating constraints," *Journal of Guidance, control, and Dynamics*, vol. 26, no. 4, pp. 523–529, 2003.

[10] A. Dwyer Cianciolo and R. W. Powell, "Entry, descent, and landing guidance and control approaches to satisfy mars human mission landing criteria," 2017.

[11] J. Davis, A. Dwyer Cianciolo, R. Powell, J. Shidner, and E. Garcia-Llama, "Guidance and control algorithms for the mars entry, descent and landing systems analysis," in *AIAA/AAS Astrodynamics Specialist Conference*, 2010.

[12] S. Dutta, A. Bowes, A. M. Dwyer Cianciolo, C. Glass, and R. W. Powell, "Guidance scheme for modulation of drag devices to enable return from low earth orbit," in *AIAA Atmospheric Flight Mechanics Conference*, 2017.

[13] C. Kluever, "Entry guidance performance for mars precision landing," *Journal of guidance, control, and dynamics*, vol. 31, no. 6, pp. 1537–1544, 2008.

[14] Z. R. Putnam and R. D. Braun, "Precision landing at mars using discrete-event drag modulation," *Journal of Spacecraft and Rockets*, vol. 51, no. 1, pp. 128–138, 2013.

[15] P. Lu, "Entry guidance: A unified method," *Journal of Guidance, Control, and Dynamics*, vol. 37, no. 3, pp. 713–728, 2014.

[16] P. Lu, B. J. Griffin, G. A. Dukeman, and F. R. Chavez, "Rapid optimal multiburn ascent planning and guidance," *Journal of Guidance, Control, and Dynamics*, vol. 31, no. 6, pp. 1656–1664, 2008.

[17] D. Lawden, "Necessary conditions for optimal rocket trajectories," *The Quarterly Journal of Mechanics and Applied Mathematics*, vol. 12, no. 4, pp. 476–487, 1959.

[18] D. F. Lawden, *Analytical Methods of Optimization*, ch. 2, pp. 36–61. Courier Corporation, 2006.

[19] H. Yang, X. Bai, and H. Baoyin, "Rapid trajectory planning for asteroid landing with thrust magnitude constraint," *Journal of Guidance, Control, and Dynamics*, vol. 40, no. 10, pp. 2713–2720, 2017.

[20] Y. Zheng, H. Cui, and Y. Ai, "Indirect trajectory optimization for mars entry with maximum terminal altitude," *Journal of Spacecraft and Rockets*, vol. 54, no. 5, pp. 1068–1080, 2017.

[21] S. Josselyn and I. M. Ross, "Rapid verification method for the trajectory optimization of reentry vehicles," *Journal of Guidance, Control, and Dynamics*, vol. 26, no. 3, pp. 505–508, 2003.

[22] P. J. Shaffer, I. M. Ross, M. W. Oppenheimer, D. B. Doman, and K. P. Bollino, "Fault-tolerant optimal trajectory generation for reusable launch vehicles," *Journal of guidance, control, and dynamics*, vol. 30, no. 6, pp. 1794–1802, 2007.

[23] T. R. Jorris and R. G. Cobb, "Three-dimensional trajectory optimization satisfying waypoint and no-fly zone constraints," *Journal of Guidance, Control, and Dynamics*, vol. 32, no. 2, pp. 551–572, 2009.

[24] J. Schierman and J. Hull, "In-flight entry trajectory optimization for reusable launch vehicles," in *AIAA guidance, navigation, and control conference and exhibit*, 2005.

[25] B. Açıkmeşe, J. M. Carson, and L. Blackmore, "Lossless convexification of nonconvex control bound and pointing constraints of the soft landing optimal control problem," *IEEE Transactions on Control Systems Technology*, vol. 21, no. 6, pp. 2104–2113, 2013.

[26] X. Liu, Z. Shen, and P. Lu, "Entry trajectory optimization by second-order cone programming," *Journal of Guidance, Control, and Dynamics*, vol. 39, no. 2, pp. 227–241, 2016.

[27] U. Lee and M. Mesbahi, "Constrained autonomous precision landing via dual quaternions and model predictive control," *Journal of Guidance, Control, and Dynamics*, vol. 40, no. 2, pp. 292–308, 2016.

[28] M. Sagliano, "Pseudospectral convex optimization for powered descent and landing," *Journal of guidance, control, and dynamics*, vol. 41, no. 2, pp. 320–334, 2018.

[29] C. Wan, R. Dai, and P. Lu, "Alternating minimization algorithm for polynomial optimal control problems," *Journal of Guidance, Control, and Dynamics*, vol. 42, no. 4, pp. 723–736, 2019.

[30] L. Vandenberghe and S. Boyd, "Semidefinite programming," *SIAM review*, vol. 38, no. 1, pp. 49–95, 1996.

[31] A. d'Aspremont and S. Boyd, "Relaxations and randomized methods for nonconvex qcqps," *EE392o Class Notes, Stanford University*, vol. 1, pp. 1–16, 2003.

[32] K. M. Anstreicher, "Semidefinite programming versus the reformulation-linearization technique for nonconvex quadratically constrained quadratic programming," *Journal of Global Optimization*, vol. 43, no. 2-3, pp. 471–484, 2009.

[33] X. Bao, N. V. Sahinidis, and M. Tawarmalani, "Semidefinite relaxations for quadratically constrained quadratic programming: A review and comparisons," *Mathematical programming*, vol. 129, no. 1, p. 129, 2011.

[34] K. M. Anstreicher, "On convex relaxations for quadratically constrained quadratic programming," *Mathematical programming*, vol. 136, no. 2, pp. 233–251, 2012.

[35] S. Boyd, N. Parikh, E. Chu, B. Peleato, J. Eckstein, *et al.*, "Distributed optimization and statistical learning via the alternating direction method of multipliers," *Foundations and Trends® in Machine learning*, vol. 3, no. 1, pp. 1–122, 2011.

[36] K. Huang and N. D. Sidiropoulos, "Consensus-admm for general quadratically constrained quadratic programming," *IEEE Transactions on Signal Processing*, vol. 64, no. 20, pp. 5297–5310, 2016.

[37] M. Hong, Z.-Q. Luo, and M. Razaviyayn, "Convergence analysis of alternating direction method of multipliers for a family of nonconvex problems," *SIAM Journal on Optimization*, vol. 26, no. 1, pp. 337–364, 2016.

[38] Y. Wang, W. Yin, and J. Zeng, "Global convergence of admm in nonconvex nonsmooth optimization," *Journal of Scientific Computing*, vol. 78, no. 1, pp. 29–63, 2019.

[39] C. Sun, N. Kingry, and R. Dai, "A unified formulation and nonconvex optimization method for mixed-type decision-making of robotic systems," *IEEE Transactions on Robotics*, vol. 37, no. 3, pp. 831–846, 2020.

[40] C. Wan, G. Jing, R. Dai, and J. R. Rea, "Fuel-optimal guidance for end-to-end human-mars entry, powered-descent, and landing mission," in *AIAA Scitech 2020 Forum*, p. 1472, 2020.

[41] NASA, "Mars atmosphere model," 2015.

[42] D. Gabay and B. Mercier, "A dual algorithm for the solution of non linear variational problems via finite element approximation," *Computers & Mathematics with Applications*, vol. 2, pp. 17–40, 1975.

[43] Y. Gu and N. Yamashita, "An alternating direction method of multipliers with the bfgs update for structured convex quadratic optimization," *arXiv preprint arXiv:1903.02270*, 2019.

[44] K. Holmström, A. O. Göran, and M. M. Edvall, "User's guide for tomlab/penopt," *Tomlab Optimization Inc*, 2006.

[45] B. P. Harper and R. D. Braun, "Preliminary design study of asymmetric hypersonic inflatable aerodynamic decelerators for mars entry," *AE8900 MS Special Problems Report, Guggenheim School of Aerospace Engineering Georgia Institute of Technology Atlanta, GA*, 2014.

Changhuang (Charlie) Wan is an assistant professor in Aerospace Science Engineering at Tuskegee University. He received bachelor and master degrees in Spacecraft Design and Engineering from Beihang University and his Ph.D. degree in in the Mechanical and Aerospace Engineering Department at The Ohio State University, Columbus, OH. His research interests include optimal control, numerical optimization, and autonomous systems.

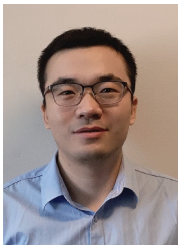

Gangshan Jing received the Ph.D. degree in Control Theory and Control Engineering from Xidian University, Xi'an, China, in 2018. From 2016 to 2017, he was a research assistant in Department of Applied Mathematics, at Hong Kong Polytechnic University. From 2018 to 2019, he was a postdoctoral researcher in Department of Mechanical and Aerospace Engineering, at Ohio State University. From 2019-2021, he was a postdoctoral researcher in Department of Electrical and Computer Engineering, at North Carolina State University. Since 2021 Dec, he has been a faculty member in School of Automation, Chongqing University, Chongqing. His research interests include distributed control, optimization, and machine learning for network systems.

Ran Dai is an associate professor in School of Aeronautics and Astronautics at Purdue University. She received her B.S. degree in Automation Science from Beihang University and her M.S. and Ph.D. degrees in Aerospace Engineering from Auburn University. Dr. Dai's research focuses on control of autonomous systems, numerical optimization, and networked dynamical systems. She is an associate editor of IEEE transaction on Aerospace and Electronic Systems, and a recipient of the National Science Foundation Career Award and NASA Early Faculty Career Award.

Jeremy Rea received a Bachelor of Science degree in Aeronautical and Astronautical Engineering from The Ohio State University in 1999 and the degree of Master of Science in Aeronautics and Astronautics from the Massachusetts Institute of Technology in 2001. He began work at the NASA Johnson Space Center in Houston, Texas in August, 2001. In 2009, he received a Doctor of Philosophy in Aerospace Engineering from The University of Texas at Austin under a Johnson Space Center Fellowship. He is currently the Orion Entry Guidance and Performance Subsystem Manager for Project Artemis and the Guidance Technical Discipline Lead at the Johnson Space Center in Houston, Texas.